Scale-Dependent Transition in Soil Moisture Memory and Its Environmental Controls in Complex Mountain Terrain

Jun Zhang[1,2,3], Songtang He[1*], Yong Li[1], Yuan Xue[2]

[1] Key Laboratory of Mountain Hazards and Engineering Resilience /Institute of Mountain Hazards and Environment, Chinese Academy of Sciences, Chengdu 610041, China

[2] State Key Laboratory of Hydroscience and Engineering; Department of Hydraulic Engineering, Tsinghua University, Beijing 100084, China

[3] University of Chinese Academy of Sciences, Beijing 100049, China

Correspondence: Songtang He (hest@imde.ac.cn)

Abstract: Soil moisture memory (SMM) – the persistence of soil moisture anomalies — is a key factor preconditioning hydrological responses and geohazard susceptibility. However, how SMM varies across timescales and the controls governing its persistence in complex terrain remain poorly understood. Here, we quantify SMM dynamics from daily to interannual scales using 20-year (2003–2022) daily soil moisture data from three contrasting watersheds in southwestern China, prone to soil erosion (Dali River Basin), shallow landslides (Anning River Basin), and debris flows (Jiangjia Ravine). Integrating Power Spectrum Analysis (persistence strength), Detrended Fluctuation Analysis (DFA-2; persistence duration), and scale-dependent attribution via Boruta random forest with partial correlation, we identify a pronounced scale-dependent transition in SMM and its drivers. SMM intensity generally weakens with increasing timescale, yet humid catchments exhibit surprisingly strong and persistent memory extending to multi-year scales. Feature importance analysis reveals a critical structural shift around the 5-year scale: short-term memory is dominated by atmospheric forcing and vegetation, whereas long-term persistence is controlled by soil properties and topography. This transition marks a conceptual shift from event-driven fast-

response (topography-mediated) to storage-dominated slow-response (soil-buffered) regimes. These findings provide a framework for distinguishing short-term hydraulic preconditioning from long-term background susceptibility, proposing a conceptual framework for incorporating memory timescales into multi-scale geohazard assessment.

Keywords: Soil moisture memory; Driving Factor; Persistence horizon; Power spectrum analysis; Detrended fluctuation analysis

1. Introduction

Soil moisture (SM) plays a critical role in mountain hazards, including debris flows, landslides, and soil erosion (An et al., 2025; Hu et al., 2015; Moragoda et al., 2022). Elevated antecedent soil moisture increases pore water pressure, reduces effective stress and shear strength, thereby lowering the critical threshold for slope failure (Bogaard et al., 2018; Cai et al., 2019). The persistence of SM—quantified by soil moisture memory (SMM)—determines how long antecedent moisture conditions influence hydraulic preconditioning, providing essential information for early warning systems (Bogaard et al., 2016; Huang et al., 2022; Wicki et al., 2020). Consequently, a comprehensive exploration of SMM and driving factors influencing it becomes imperative for effective natural hazard prevention and water resources management (Dobriyal et al., 2012; Wicki et al., 2020).

Soil moisture memory (SMM) ranges from days to years and is controlled by various factors (e.g., atmospheric forcing, soil properties, vegetation, and topography) (Entin et al., 2000; McColl et al., 2017; Rahmati et al., 2024). In mountain catchments, the pronounced spatial heterogeneity of

47 these factors increases the sensitivity of hazard initiation to antecedent moisture while shortening
48 hydrological response times (Bogaard & Greco, 2016; Dymond et al., 2021; Wicki et al., 2020). For
49 instance, landslide probability increases exponentially once soil moisture exceeds critical thresholds
50 of ~30–40 % (Mirus et al., 2018; Wicki et al., 2021), with slope angle acting as a key topographic
51 modulator. For debris flows, antecedent soil moisture influences not only initiation probability, but
52 also runout distance (Coe et al., 2008). Similarly, soil loss rates under wet antecedent conditions can
53 be 3–5 times higher than under dry conditions at equivalent rainfall intensities (Ran et al., 2012).
54 Despite this established importance, systematic studies tracing SMM evolution across contiguous
55 timescales—from monthly to seasonal, annual, and multi-year—remain scarce, particularly in steep
56 mountain terrain (Entin et al., 2000; Nicolai-Shaw et al., 2016; Zhang et al., 2025). Additionally,
57 unraveling the mechanisms behind SMM variation is challenging due to the complex interplay of
58 topographic, pedological, meteorological, and vegetation controls (Brocca et al., 2007; Dong et al.,
59 2018; Peng et al., 2023; Schönauer et al., 2024; Varga et al., 2020). Therefore, our study focuses on
60 mountainous areas prone to natural hazards, aiming to quantify SMM variations and identify the
61 dominant controlling factors across multiple timescales.

62 Furthermore, previous studies have explored driving factors of soil moisture variability at
63 discrete temporal scales (Blanka-Végi et al., 2025; Cho et al., 2014; Fang et al., 2016; Kursa et al.,
64 2010). For instance, Blanka-Végi et al. (2025) identified wilting point and evapotranspiration as key
65 factors influencing SM at the annual scale using machine learning algorithms (MLR, SVR,
66 XGBoost, and DNN). Similarly, other studies have demonstrated that vegetation type, soil texture,
67 and precipitation also affect SMM (Brocca et al., 2012; Fang et al., 2016; Zhang et al., 2021, 2025).
68 Nevertheless, the factors governing SMM across various temporal scales have received limited

investigation, particularly in mountain areas. The mechanism that multi-scale SMM influence mountain hazard initiation and development remains largely unexplored.

In this study, we selected three catchments—Dali River Basin, Anning River Basin, and Jiangjia Ravine (representing distinct hazard regimes) — to research SMM characteristics and their scale-dependent drivers. The Power Spectrum Analysis (PSA) was used to investigate SMM characteristics. Subsequently, we employed DFA-2 method to identify characteristic persistence timescales. Moreover, to quantify the influence of environmental drivers, we employed scale-dependent attribution based on Boruta random forest combined with partial correlation analysis. Leveraging a two-decade daily soil moisture dataset, this study aims to: (1) quantify the scale-transition threshold and hierarchical drivers of SMM; (2) establish a quantitative hierarchy of driving factors across temporal scales; and (3) propose a conceptual framework that links multi-scale SMM to differentiated hazard preconditioning mechanisms, providing testable hypotheses for future event-based validation. The paper is structured as follows: Section 2 describes the study areas, data, and methods. Section 3 presents the results; Section 4 provides the discussion; and Section 5 summarizes the main conclusions.

2. Materials and Methods

This study investigates soil moisture (SM) dynamics and their drivers across three hydro-climatically and geomorphologically distinct watersheds: the Dali River Basin, Anning River Basin, and Jiangjia Ravine. The Dali River Basin, located on the Loess Plateau, represents a semi-arid erosion-dominated system where soil moisture deficits and intense summer storms drive severe soil loss (Liu et al., 2023). The Anning River Basin and Jiangjia Ravine, located in southwestern China—a global hotspot for rainfall-triggered landslides and debris flows due to complex terrain,

active tectonics, and intense monsoon precipitation (Wei et al., 2025; Yang et al., 2023)—represent humid landslide-prone and high-frequency debris flow environments, respectively. This gradient design spanning semi-arid to humid climates and erosion to mass-movement hazards enables identification of both commonalities and differences in SMM mechanisms across contrasting mountain environments. We incorporated static and dynamic variables—spanning topography, soil properties, meteorological conditions, and vegetation indices—from multiple authoritative datasets. SM temporal memory and persistence horizons were quantified using Power Spectral Analysis (PSA) and second-order Detrended Fluctuation Analysis (DFA-2), respectively, while the Boruta–Random Forest algorithm was employed to quantify variable importance across spatial and temporal scales. The integrated use of these methods is designed to address complementary aspects of our research questions:

- Power Spectral Analysis (PSA) is used to characterize the overall distribution of SM variance across timescales (from daily to interannual), identifying the dominant frequencies of variability (Kantelhardt et al., 2006; Parada et al., 2003).
- Second-order Detrended Fluctuation Analysis (DFA-2) is specifically chosen to robustly quantify long-range persistence (memory) and to distinguish it from short-term correlations, providing a direct measure of the memory timescale (τ_{SMM}) (Kantelhardt et al., 2001; Zhang et al., 2025).
- The Boruta–Random Forest algorithm serves to identify and rank the key drivers (both static and dynamic) of SM memory across different temporal scales, handling high-dimensional data and complex, non-linear interactions without prior assumptions about variable relationships (Breiman, 2001; Kursa et al., 2010).

Together, this multi-method framework allows us to not only quantify how strong and how long SM memory persists, but also to attribute why it varies across scales and locations (Fig. 1).

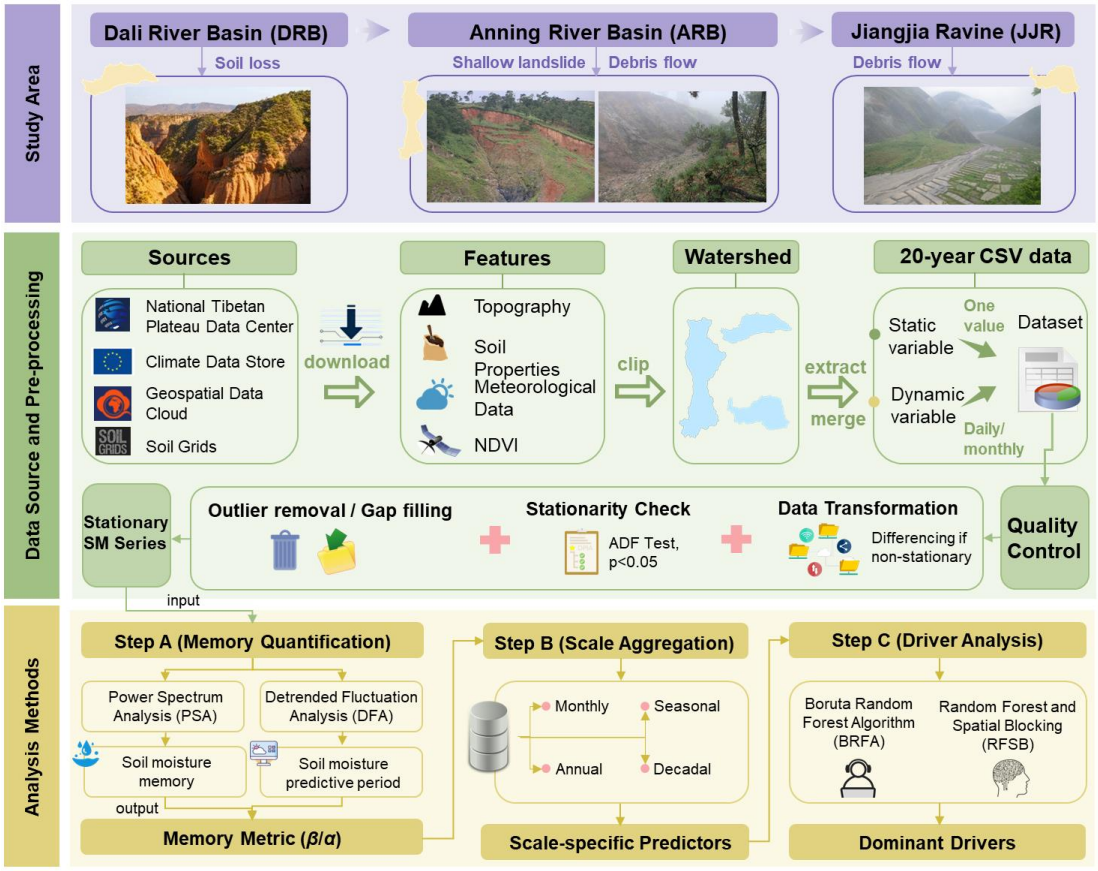

Fig. 1 Schematic workflow of the multi-scale soil moisture memory (SMM) analysis framework. The framework comprises three stages: (1) data preparation, where multi-source static (topography, soil) and dynamic (meteorology, vegetation) variables are harmonized and soil moisture time series undergo quality control and stationarity verification; (2) memory quantification, using Power Spectral Analysis (PSA) to characterize variance distribution across frequencies and Detrended Fluctuation Analysis (DFA-2) to derive memory timescales; and (3) driver attribution, applying the Boruta-Random Forest algorithm to identify scale-dependent importance of controlling factors. This integrated workflow resolves the strength, duration, and controls of SMM across timescales.

The overall research framework is shown in Figure 1, outlining the data flow, analysis steps, and their complementary roles in the multi-scale quantification and attribution of SMM.

2.1 Study Area

We selected three hydro-climatically distinct watersheds in southwestern China to represent a spectrum of mountain hazard environments (Fig. 2; detailed physiographic characteristics are provided in Appendix B and Table B1). These three basins were purposefully selected to cover a diverse range of hydro-climatic conditions (semi-arid to humid) and geomorphic types (loess plateau to steep tectonic valleys), allowing for a robust comparative analysis of SMM drivers across contrasting mountain terrains.

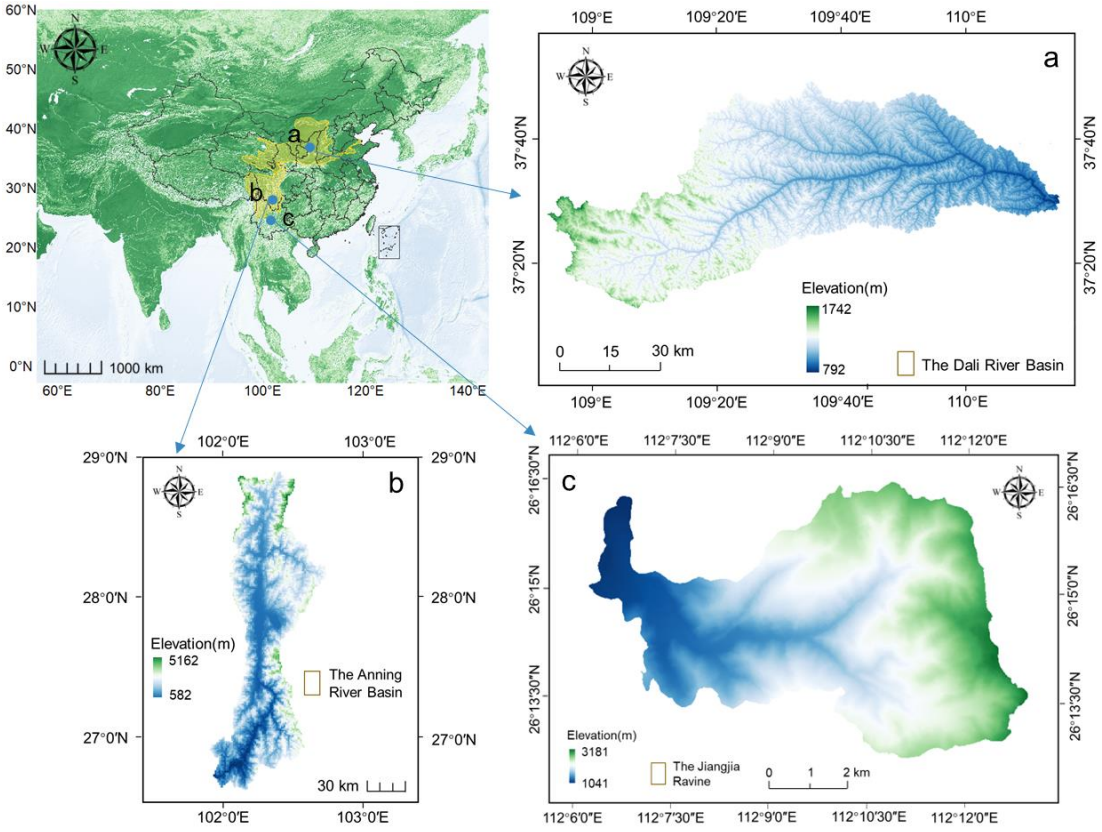

Fig. 2 Location of the study areas: (a) the Dali River Basin (DRB), (b) the Anning River Basin, (c) the Jiangjia Ravine.

- **Dali River Basin (DRB):** Semi-Arid Erosion-Prone System. Located on the Chinese Loess Plateau (3,906 km^2), the DRB features steep loess terrain (avg. slope 17°) and

highly erodible soils (silt > 60 %). The climate is semi-arid continental, with precipitation highly concentrated in summer storms (> 70 % from May to September), leading to persistent soil moisture deficits and severe erosion rates (Liu et al., 2023; Zhang et al., 2023).

- **Anning River Basin (ARB):** Complex Mountain-Valley System. Situated in southwestern Sichuan (11,150 km^2), the ARB is characterized by dramatic relief (900–4,750 m) and vertical climatic zonation. It operates under a humid subtropical-monsoon climate (~ 1,070 mm rainfall) with dense forest cover (Chen et al., 2024). Consequently, soil moisture dynamics are strongly regulated by vegetation phenology and the buffering capacity of deep forest soils (Yin et al., 2020).
- **Jiangjia Ravine (JJR):** Debris-Flow Dominated Catchment. A small (48.6 km^2) but extremely steep catchment in the Xiaojiang fault zone. Intense monsoon rainfall (> 85 % in May–Oct) combined with fractured geology drives rapid hydrological response cycles: rapid saturation during storms followed by quick drainage (Yang et al., 2023). This makes JJR a classic environment for high-frequency debris flows (Wei et al., 2025).

Despite the large difference in basin area (ARB: 11,150 km^2 vs. JJR: 48.6 km^2), a scale-matching sensitivity analysis (Appendix H) confirms that the observed differences in soil moisture memory between basins reflect intrinsic hydrological and landscape characteristics rather than artifacts of spatial averaging or domain size.

2.2 Data Sources and Preprocessing

We constructed a dataset comprising 12 static and dynamic covariates (Table 1) alongside daily soil moisture (SM) data (1-km resolution) for 2003–2022. These covariates were selected based on

an extensive literature review of soil moisture drivers (Rahmati et al., 2024; Seneviratne et al., 2010), prioritizing variables that are (1) widely recognized as key controls on SMM (topography, soil properties, meteorology, vegetation), (2) frequently used in prior multi-scale SMM studies, and (3) available at consistent spatial and temporal resolution with high reliability across the study region.

Soil Moisture Dataset: We utilized the all-weather 1-km daily soil moisture (SM) product developed by Song et al. (2022). This dataset employs a machine learning-based spatiotemporal reconstruction framework to generate seamless high-resolution estimates by downscaling and fusing coarse-resolution passive microwave observations (AMSR-E/2) with high-resolution optical/thermal land surface parameters (MODIS) and meteorological forcing (ERA5-Land), using a random forest algorithm trained on extensive ground observations.

Validation and Uncertainty: This product was selected for its capacity to resolve hillslope-scale heterogeneity in complex terrain, a critical requirement for our hazard-focused analysis. Comprehensive validation against approximately 2,400 in-situ stations across China demonstrates robust accuracy, with an average correlation coefficient (R) of 0.89 and an unbiased Root Mean Square Error (ubRMSE) of 0.053 m^3/m^3 (Song et al., 2022). While inherent uncertainties exist in microwave retrieval in mountainous regions (e.g., geometric distortion and shadowing effects), this dataset represents the optimal balance between spatial resolution and temporal continuity. Furthermore, since our study focuses on the temporal persistence features (spectral exponents) rather than absolute magnitudes, the potential systematic bias in complex terrain has minimal impact on the derived memory metrics (see Appendix C for further discussion on data reliability and preprocessing).

Table 1. Static and dynamic covariates used in the final modeling framework and the target variable

(soil moisture, SM).

Types	Variable (abbreviation)	Description	Units	Source
Static	Slope (θ)	Rate of change of elevation at each pixel (DEM-derived)	°	Geospatial Data Cloud (DEM)
	Aspect (Asp)	Orientation of the steepest downslope (DEM-derived)	°	
	Topographic Wetness Index (TWI)	Potential wetness index based on slope and upslope contributing area (DEM-derived)	-	
	Soil texture (Sand, Silt, Clay)	Mass fractions of soil particle-size classes	g/kg	Soil Grids
	Normalized Difference Vegetation Index (NDVI)	Vegetation greenness from red and NIR reflectance	-	Gao et al., 2022
Dynamic	Precipitation (Prec.)	Daily total precipitation	mm	Xie et al., 2019
	Surface wind speed (WS)	Mean daily wind speed at 10 m height	m/s	ERA5 (Hersbach et al., 2023)
	Relative humidity (rhu)	Ratio of actual to saturated vapor pressure	%	
	2m air temperature (T_{2m})	Daily mean air temperature at 2 m height	℃	
	Actual evaporation (AE)	Daily actual evapotranspiration	mm/day	
Target	Soil moisture (SM)	Volumetric soil water content	cm^3/cm^3	Song et al., 2022

Static variables (e.g., soil texture, TWI) represent basin physiography, while dynamic variables (e.g., precipitation, NDVI) capture climate-vegetation interactions. All data were resampled to a uniform 1-km grid. Preprocessing included linear interpolation for short gaps (≤ 3 days), outlier removal, and stationarity checks using the Augmented Dickey-Fuller test (details in Appendix C).

2.3 Quantifying Soil Moisture Memory (PSA and DFA-2)

To characterize the multi-scale persistence of soil moisture, we employed two complementary spectral techniques that quantify long-range temporal correlations. Power Spectrum Analysis (PSA)

identifies memory strength across frequency domains, while Detrended Fluctuation Analysis (DFA-2) detects the timescales over which memory persists. Both methods are robust to non-stationarity and can distinguish genuine long-term correlations from short-term noise or trends (Kantelhardt et al., 2006; Zhu et al., 2010).

Given the 20-year record length (2003–2022), statistical limitations exist for resolving low-frequency dynamics. Following established guidelines requiring $N \geq 3T$ for robust spectral estimation (Ghannam et al., 2016; Percival & Walden, 1993), we distinguish between two regimes:

1. **Reliable Spectral Window ($T \leq 7$ years):** Timescales up to $T = N/3 \approx 6.7$ years (rounded to 7 years) can be reliably estimated, as our record contains at least three complete cycles.
2. **Low-Frequency Background State ($T > 7$ years):** Signals at these timescales reflect slow-varying boundary conditions (e.g., multi-year drought periods) rather than event-scale memory. These estimates have lower statistical confidence and are interpreted as qualitative indicators of long-term storage trends.

Power Spectral Analysis (PSA). PSA decomposes a time series into its constituent frequencies, estimating how variance (power) is distributed across them. The relationship follows a power law: $S(f) \sim f^{-\beta}$, where $S(f)$ is the spectral power at frequency f, and β is the spectral exponent. A higher β indicates that low-frequency (long-term) variations dominate the signal, implying stronger soil moisture memory. In this study, β values within the Reliable Spectral Window (seasonal to ~7 years) quantify interannual persistence, while those in the Low-Frequency Background (>7 years) indicate quasi-static mean-state stability.

Detrended Fluctuation Analysis (DFA-2). To account for non-stationarity, we applied second-order DFA-2. It quantifies long-range correlations by analyzing how the root-mean-square

fluctuation $F(s)$ of the integrated series scales with window size s: $F(s) \sim s^{\alpha}$. The fluctuation exponent α indicates the correlation structure: $\alpha = 0.5$ corresponds to uncorrelated white noise; $\alpha > 0.5$ indicates persistent long-range correlations; and $\alpha = 1.0$ represents scale-invariant $1/f$ noise (Kantelhardt et al., 2001). DFA-2 filters out polynomial trends to reveal intrinsic correlations, making it suitable for non-stationary hydrological records. Cross-validation with the standard Autocorrelation Function confirms the robustness of these metrics (Appendix E, Fig. E1).

We defined the "persistence horizon" as the range of timescales over which $\alpha \geq 0.9$, indicating strong long-range memory approaching scale-invariant behavior. In this study, persistence horizon is used as the operational measure of memory length, specifically denoting the temporal range where significant long-range memory ($\alpha \geq 0.9$) is maintained. This threshold follows established criteria in hydroclimatic memory studies (Zhang et al., 2025; Zhu et al., 2010). Physically, it represents the temporal window over which antecedent moisture conditions influence the current state—a critical parameter for hazard preconditioning. Persistence horizons extending beyond 7 years reflect slow-changing baseline conditions rather than event-scale memory. Detailed formulations and significance testing are provided in Appendix A.

For clarity, key terms are defined as follows:

- **Soil Moisture Memory (SMM):** The tendency of soil moisture anomalies to persist over time following wetting or drying events. SMM is quantified by the spectral exponent β (memory strength) and fluctuation exponent α (memory timescale).
- **Significant Memory:** A state where $\alpha \geq 0.9$, indicating strong long-range correlations.
- **Persistence Horizon:** The timescale range (in days) over which significant memory is observed.

2.4 Identifying Predictors via a Spatial Attribution Modeling Framework

To determine the hierarchical importance of environmental predictors, we utilized the Boruta feature selection algorithm wrapped around a Random Forest regressor. Boruta is an all-relevant feature selection method that creates randomized "shadow" copies of original predictors (permuted versions with no real relationship to the target) and iteratively compares the importance of each real predictor against the best-performing shadow variable. Predictors that consistently outperform shadow variables are retained as relevant, while others are rejected (Kursa & Rudnicki, 2010). Boruta was selected because it (1) captures non-linear relationships inherent in soil-vegetation-atmosphere systems, (2) handles collinearity among predictors without requiring prior variable removal, and (3) provides statistically validated importance rankings by comparing against a null model.

Given that SMM is a temporal statistic derived from time series, while landscape attributes are spatially heterogeneous, we constructed a spatial attribution framework to link these dimensions, quantifying how driver importance shifts across different temporal aggregation windows (monthly to decadal). Specifically, the temporal memory metric for each pixel (e.g., spectral exponent β) serves as the spatial response variable, regressed against spatially distributed predictors:

1. **Static variables:** Landscape properties constant over the study period (e.g., soil texture, slope, TWI).
2. **Aggregated dynamic variables:** Time-varying meteorological and vegetation data aggregated to match the temporal scale of the memory metric (e.g., mean decadal NDVI or total precipitation).

This framework quantifies how spatial heterogeneity in static and dynamic boundary

conditions correlates with temporal persistence of soil moisture. Feature importance was validated using spatial block cross-validation to account for spatial autocorrelation (details in Appendix D).

2.5 Methodological Considerations and Limitations

The "Space-for-Time" framework leverages spatial heterogeneity across the three watersheds as a substitute for long-term temporal observations at a single site, an approach widely adopted in ecological and hydrological studies (Pickett, 1989). However, this approach identifies statistical associations rather than causal relationships. The Boruta-RF algorithm ranks predictors by their capacity to explain spatial variance in temporal memory metrics, but cannot distinguish between direct causal drivers, proxy variables, or feedback responses. Therefore, associations should be interpreted as indicative of likely controls rather than confirmed causal mechanisms (McColl et al., 2017; Seneviratne et al., 2010).

Additionally, physical collinearity inherent in mountain landscapes—often described by the catena concept of co-evolved soil-topography relationships (i.e., steep upper slopes have thin, sandy, fast-draining soils while gentle lower slopes accumulate thick, clay-rich, water-retaining soils; Anderson, 2005)—means that high importance scores for both Slope and Clay content (Section 3.3) likely reflect coupled landscape structure rather than independent effects.

To address these limitations, we (1) interpret associations through established hydrological theory (e.g., linear reservoir models; Section 4.1) to provide mechanistic plausibility, and (2) conduct partial correlation analysis controlling for topographic variables (Appendix G) to assess robustness against landscape confounding. This framework generates testable hypotheses about SMM predictors rather than confirming causal mechanisms, which would require controlled experiments beyond the scope of this study.

3. Results

3.1 Power Spectrum Analysis of SM Memory

Power spectrum analysis revealed scale-dependent characteristics of soil moisture memory (SMM) across the three basins (Fig. 3). Quantitative interpretations focus on the Reliable Spectral Window (≤ 7 years), while longer timescales reflect quasi-stationary moisture regimes.

In Figure 3, the x-axis represents frequency (cycles per year, logarithmic scale) and the y-axis represents spectral power $S(f)$ (log-transformed). The spectral exponent β corresponds to the negative slope of the fitted line: higher β indicates variance concentrated at low frequencies, implying strong memory, while lower β indicates high-frequency dominance characteristic of weak memory. Shaded bands represent 95 % confidence intervals. Three key patterns emerge: (1) intra-annual contrasts between wet and dry seasons, (2) systematic decline in memory strength with increasing timescale, and (3) inter-basin differences reflecting contrasting hydro-climatic regimes. For seasonal classification, the rainy and dry seasons are defined based on local precipitation regimes: the Dali River Basin (DRB) rainy season spans July to September (dry season: October–June), while both the Anning River Basin (ARB) and Jiangjia Ravine (JJR) share a rainy season from May to October (dry season: November–April).

Intra-annual patterns: Analysis compared individual months with integrated seasonal periods (Fig. 3a–1, b–1, c–1) (Detailed definitions and analytical methods are provided in Appendix D). This revealed asymmetric patterns: memory during individual rainy season months was consistently weaker than the integrated rainy season, whereas individual dry season months showed stronger memory than the dry season aggregate. For example, in the ARB, the integrated rainy season yielded $\beta = 2.190 \pm 0.101$, while individual rainy months averaged $\beta = 2.179 \pm 0.095$; conversely, individual

dry season months (β = 2.698 ± 0.121) exceeded the integrated dry season (β = 1.643 ± 0.051).

Interannual patterns: SMM declined progressively at longer timescales. Within the reliable window, the hierarchical trend follows β(1-yr) > β(5-yr). Beyond 7 years, metrics stabilized, capturing the basin's static storage baseline (Fig. 3a–2, b–2, c–2).

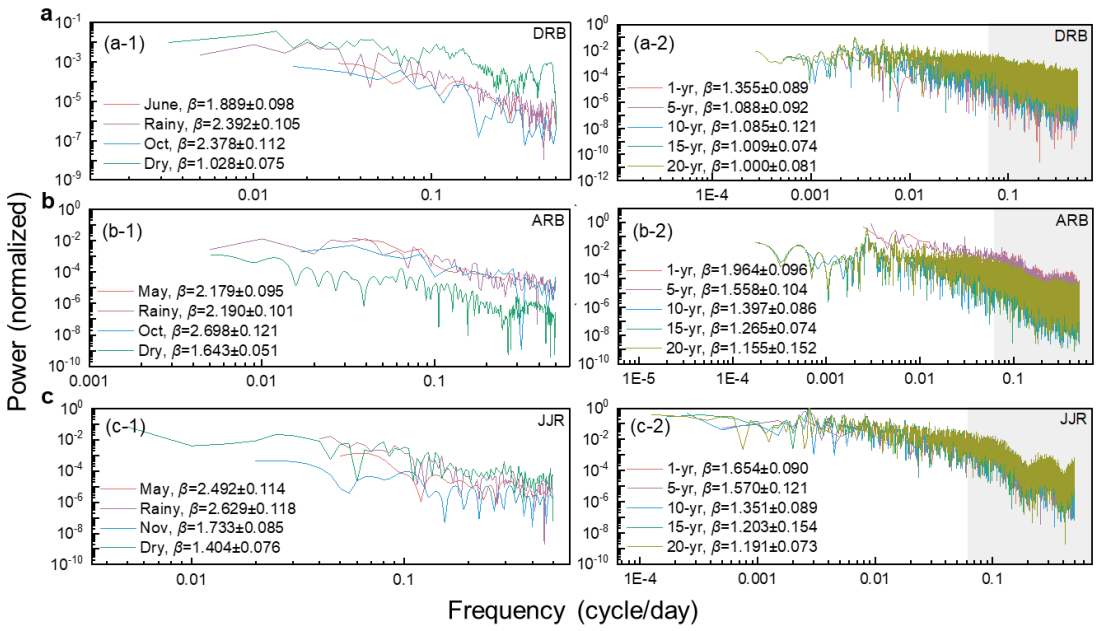

Fig. 3 Power spectrum analysis of soil moisture memory in the (a) Dali River Basin (DRB), (b) Anning River Basin (ARB), and (c) Jiangjia Ravine (JJR). Left panels show intra-annual spectra (months and aggregated seasons); right panels show inter-annual spectra (1–20 years). The spectral exponent β (mean ± 95% CI) is derived from linear regression in log-log space, where steeper slopes indicate stronger memory. Gray shading denotes timescales >1825 days, where spectral estimation is limited by record length; estimates beyond the ~7-year scale should be interpreted as low-frequency background trends rather than statistically robust memory features. Key findings: rainy season memory exceeds dry season memory; β decreases with increasing timescale; ARB shows the strongest memory, followed by JJR and DRB.

In the Dali River Basin (DRB), full rainy season memory (β = 2.392 ± 0.105) was significantly stronger than the initial month (June, β = 1.889 ± 0.098), indicating pronounced long-range

persistence where cumulative monsoon rainfall progressively builds hydrological inertia (Rahmati et al., 2024). Conversely, integrated dry season memory (β = 1.028 ± 0.075) was weaker than October (β = 2.378 ± 0.112) (Fig. 3a-1), reflecting residual moisture persisting into early autumn before rapid depletion. At interannual scales, SMM declined from β = 1.355 ± 0.089 (1-year) to β = 1.000 ± 0.081 (20-year) (Fig. 3a-2), indicating limited carryover beyond a few years. For erosion hazards, antecedent moisture from preceding weeks to months—rather than years—is most relevant for modulating soil erodibility (Ran et al., 2012). We explain the rationale for selecting June and October in Appendix B.

In the Anning River Basin (ARB), integrated rainy season memory (β = 2.190 ± 0.101) was slightly stronger than May (β = 2.179 ± 0.095), peaking in October (β = 2.698 ± 0.121) (Fig. 3b-1). High β values reflect strong persistence driven by accumulated monsoon precipitation and the buffering capacity of deep forest soils (Bogaard & Greco, 2018). At interannual scales, the ARB exhibited the highest SMM among basins (mean β = 1.468 ± 0.084), decreasing from 1.964 ± 0.096 (1-year) to 1.265 ± 0.074 (20-year) (Fig. 3b-2). This sustained multi-year memory suggests wet years can progressively elevate baseline pore pressures, potentially lowering landslide triggering thresholds (Cui et al., 2025).

In Jiangjia Ravine (JJR), SMM peaked during the rainy season (May: β = 2.492 ± 0.114; full rainy season: β = 2.629 ± 0.118) and weakened during the dry season (Nov: β = 1.733 ± 0.085; full dry season: β = 1.404 ± 0.076) (Fig. 3c-1). This strong seasonal contrast reflects rapid hydrological response: frequent monsoon rainfall maintains elevated moisture and strong autocorrelation, while steep terrain promotes quick drainage during dry periods. At interannual scales, JJR exhibited intermediate SMM—stronger than DRB but weaker than ARB—with β decreasing from 1.654 ±

346 0.090 (1-year) to 1.191 ± 0.073 (20-year) (Fig. 3c-2). For debris flow hazards, antecedent wetness
347 from preceding days to weeks within the rainy season is critical (Wei et al., 2025), whereas inter-
348 annual carryover is less pronounced than in the forest-buffered ARB.

349 In summary, SMM is consistently stronger in rainy seasons than in individual months and
350 weakens progressively toward a climate-driven baseline. The ARB shows the strongest overall
351 memory, highlighting how basin characteristics shape persistence beyond short-term weather
352 effects—with clear relevance for multi-scale hazard prediction.

353 **3.2 DFA-2 Analysis of SM Persistence Horizons**

354 Building on the PSA results, we quantified persistence horizons using DFA-2. While β
355 characterizes overall memory strength, the fluctuation exponent α identifies specific timescales
356 where memory is strongest ($\alpha \geq 0.9$). All reported α values in this range were statistically significant
357 ($p < 0.01$) based on phase-randomization surrogate testing (see Appendix A).

358 Figure 4 presents DFA-2 results organized by basin (rows: a = DRB, b = ARB, c = JJR) and
359 timescale (columns: left = seasonal, right = inter-annual). Solid lines show how α varies with
360 window size s; labeled time windows (e.g., "236–728 d") indicate persistence horizons where $\alpha \geqslant$
361 0.9.

362 In the Dali River Basin (DRB), persistence was short during the early rainy season (24–30 days
363 in June) but extended substantially through the full rainy season (41–122 days); October exhibited
364 negligible persistence, with α falling below the 0.9 threshold (Fig. 4a-1). This indicates rapid decay
365 of moisture anomalies due to intense evaporative drying following monsoon withdrawal. During
366 the dry season, persistence increased to 61–95 days, reflecting conditions where moisture decay is
367 governed primarily by intrinsic drainage properties rather than evaporative demand (Seneviratne et

al., 2010). At interannual scales, persistence horizons increased from 31–73 days (1-year) to 174–429 days (20-year), peaking between 10 and 15 years (Fig. 4a-2). This pattern is consistent with deeper-layer memory and reduced influence of high-frequency atmospheric forcing at longer timescales (Rahmati et al., 2024).

The Anning River Basin (ARB) exhibited the longest persistence horizons across all temporal scales ($p < 0.05$). At the monthly scale, persistence ranged from 17–31 days in May to 25–31 days in October, increasing markedly at the seasonal scale—reaching 37–184 days during the rainy season and 47–76 days during the dry season (Fig. 4b-1). At interannual scales, persistence horizons rose sharply from 40–71 days (1-year) to 236–728 days (20-year) (Fig. 4b-2). This extended memory implies that the basin's soil moisture state integrates cumulative effects of multi-year climate variability rather than responding solely to individual storm events. Consequently, a sequence of wet years progressively saturates deep soil layers, elevating background pore pressures—a critical factor for landslide susceptibility assessment.

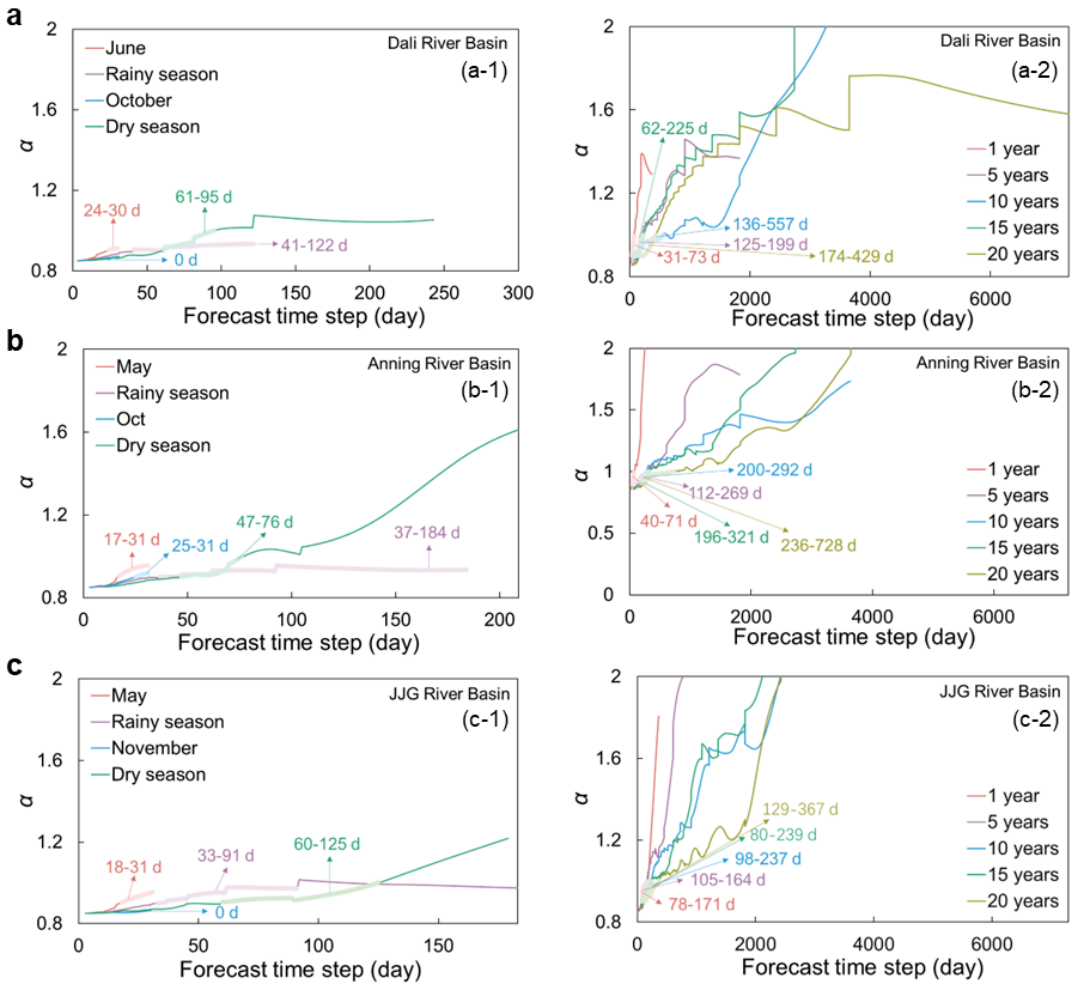

Fig. 4 DFA-2 analysis of soil moisture persistence across (a) Dali River Basin (DRB), (b) Anning River Basin (ARB), and (c) Jiangjia Ravine (JJR). Left panels: seasonal scales; right panels: inter-annual scales (1–20 years). Solid lines represent the fluctuation exponent α; labeled time windows indicate persistence horizons where $\alpha \geq 0.9$. ARB shows the longest persistence (up to 728 days), JJR the shortest rainy-season persistence (18–31 days), and DRB intermediate values. Sensitivity tests are detailed in Appendix E.

In Jiangjia Ravine (JJR), rainy season persistence was the shortest among the three basins (18–31 days in May; 33–91 days when aggregated), indicating rapid response to precipitation inputs (Fig. 4c-1). This 2–4 week persistence horizon defines the critical "look-back window" for debris flow early warning (Pan et al., 2018; Wicki et al., 2020). In contrast, dry season persistence (60–125 days) was longer, reflecting reduced evaporative demand when rainfall ceases. At interannual

scales, persistence horizons remained stable, ranging from 78–171 days (1-year) to 129–367 days (20-year) (Fig. 4c-2), suggesting that intrinsic drainage characteristics impose a consistent upper bound on moisture retention regardless of climatic variability.

Persistence horizons vary markedly across basins: longest in ARB (months to years), shortest in JJR during the rainy season (2–4 weeks), and intermediate in DRB. These time windows define practical "look-back" periods for anticipating different mountain hazards, from short-term debris flows to longer-term landslide preconditioning.

3.3 Driving Factor Selection

The Boruta Random Forest Algorithm identified statistical associations between environmental variables and SMM across multiple timescales (Fig. 5). Variables were classified as "confirmed" (Z-score significantly exceeds shadow maximum, $p < 0.01$), "tentative" (borderline significance), or "rejected." Bootstrap resampling ($n = 1000$) confirmed that top predictors at each scale maintained significance across > 95 % of iterations.

Monthly to seasonal scales: June—the onset of the rainy season—showed no distinct dominant predictor. However, when the entire rainy season (Jun–Sep) was considered, relative humidity (rhu), NDVI, actual evaporation (AE), and 2-m air temperature (T_{2m}) emerged as the strongest predictors of SMM spatial patterns. During the dry season (Oct–May), NDVI, AE, rhu, and T_{2m} maintained strong associations with SMM, whereas precipitation and wind speed exhibited limited predictive power, reflecting the transition from moisture-limited to energy-limited evapotranspiration regimes.

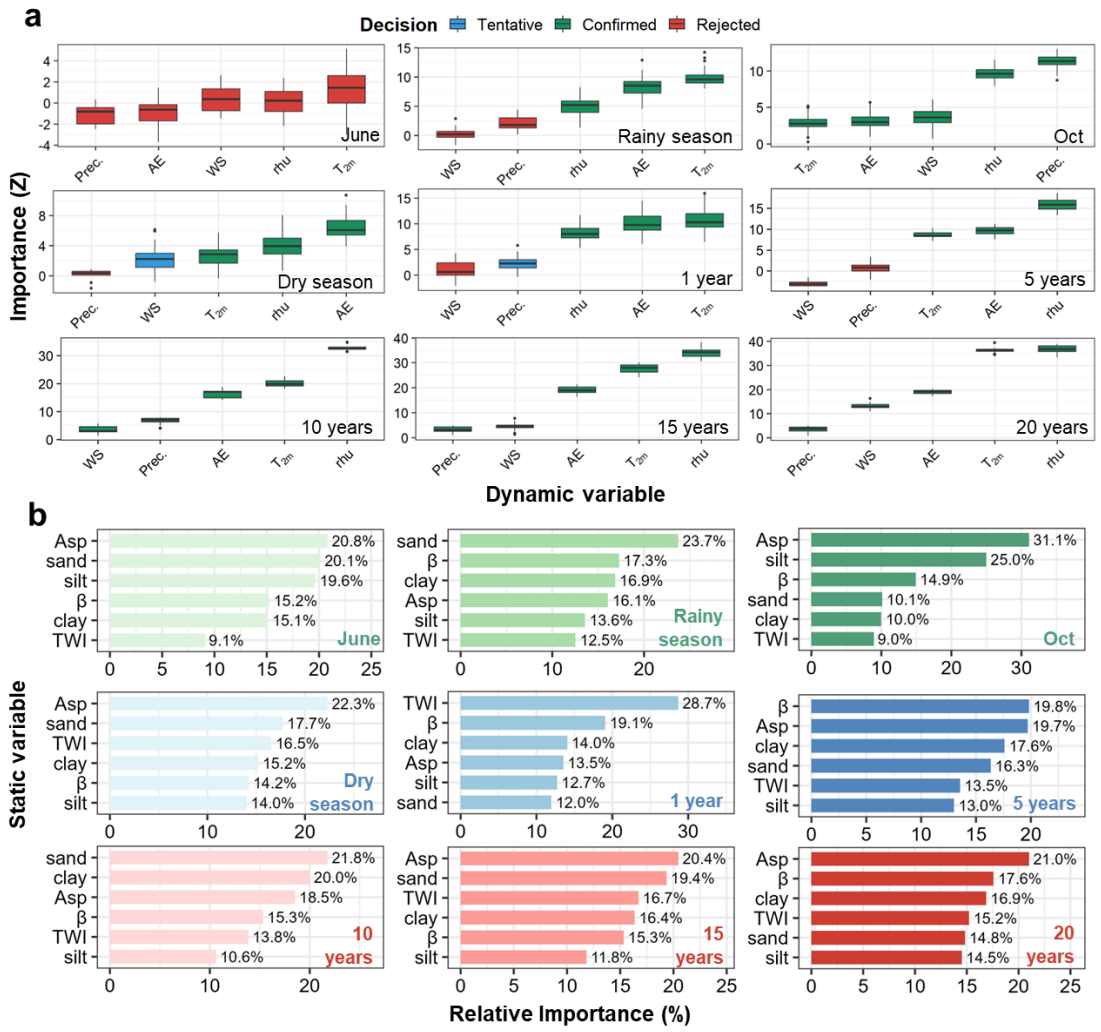

Fig. 5 Scale-dependent predictive importance of environmental drivers for soil moisture memory from monthly to decadal timescales. (a) Dynamic drivers evaluated by Boruta algorithm (*Z*-scores; green: confirmed, yellow: tentative, red: rejected; $p < 0.01$). (b) Static drivers assessed by Random Forest (relative importance, %). Note: Panels (a) and (b) use different metrics and are not directly comparable. Abbreviations: Prec., precipitation; WS, wind speed; rhu, relative humidity; T_{2m}, 2-m air temperature; AE, actual evapotranspiration; NDVI, normalized difference vegetation index; TWI, topographic wetness index; Asp., aspect; ρ_b, bulk density.

Annual to decadal scales: The pattern of associations underwent progressive transition. The cumulative importance of atmospheric variables (Precipitation, Wind Speed, T_{2m}, rhu) declined from 62 % at the monthly scale to 34 % at the 10-year scale, while soil texture variables (Sand, Silt, Clay) increased from 12 % to 38 % (Fig. 5). At annual scales, precipitation and wind speed declined

in importance as temporal averaging smoothed their high-frequency variability. By the 5-year scale, these climatic variables were excluded from significant predictors, leaving NDVI, rhu, AE, and T_{2m} as dominant variables. Over decadal timescales (10–20 years), associations of NDVI, rhu, and T_{2m} with SMM further intensified.

Static factors: The relative importance of static factors also varied with timescale (Fig. 5b). During June and the rainy season, bulk density (ρ_b) and aspect (Asp) showed the strongest associations. At annual scales, topographic associations (TWI) strengthened. However, over longer timescales, pedological factors became increasingly prominent.

Scale-transition threshold: Quantitative analysis revealed a distinct structural break at the 5-year scale (Table 2). At the 1-year scale, TWI showed the strongest association (28.7 %), consistent with topography-driven lateral water redistribution. At the 5-year scale, TWI importance declined (to 13.5 %), with the hierarchy shifting to Soil Texture and Slope (~19 %). This threshold reflects a fundamental shift from event-scale hydraulic connectivity ("Fast-Response Regime") to long-term pedological storage control ("Background-Storage Regime") (Blöschl & Sivapalan, 1995; Western et al., 2004).

Table 2. The structural shift in dominant statistical associations across timescales.

Time Scale	Top Static Predictor (Importance %)	Top Dynamic Predictor (Importance *Z*)	Association Pattern
1-Year	TWI (28.7%)	T_{2m} (11.2)	Topography-Associated (Water redistribution)
5-Year	β/Asp (~19.8%)	rhu (16.1)	Transition Point (TWI collapses; Structure stabilizes)
10-Year	Sand (21.8%)	rhu (32.5)	Soil-Texture Associated (Storage capacity)
20-Year	Asp (21.0%)	rhu (36.2)	Soil-Texture Associated

***Note*:** Seasonal scales (e.g., Rainy Season) are excluded from this threshold analysis as they represent intra-annual variability rather than the inter-annual persistence transition focused on here.

"Predictor" and "Associated" terminology is used to reflect statistical relationships; causal interpretations require additional mechanistic validation (see Section 2.4 and Section 4.1).

Methodological considerations: These associations do not establish causal relationships. The Boruta-RF algorithm identifies variables with strong predictive power but cannot distinguish between direct causal drivers, proxy variables, or bidirectional feedbacks. For instance, the strong NDVI–SMM association at decadal scales may reflect vegetation's influence on soil hydraulic properties, soil moisture's constraint on vegetation growth, or both. Mechanistic interpretation is discussed in Section 4.1. Partial correlation analysis controlling for topographic variables (Appendix G) indicated that soil texture maintained significant associations with decadal-scale SMM (partial $r = 0.43$, $p < 0.01$) after accounting for slope and TWI, though effect size was reduced compared to raw correlation ($r = 0.61$), suggesting approximately 30 % of the apparent association may be attributable to topographic confounding.

Short-term memory is driven primarily by weather and vegetation factors, whereas beyond ~5 years, soil texture and topography become dominant. This scale-dependent shift from dynamic to static control marks a fundamental transition in SMM mechanisms—essential for developing timescale-appropriate hazard models.

3.4 Cross-Basin Comparison of Memory and Drivers

To address basin-specific memory characteristics relevant to mountain hazards, we synthesized SMM properties and dominant controls across the three watersheds. Key metrics—spectral exponent (β), DFA-2 predictive period, and the top three driving factors—at monthly, annual, and decadal scales are summarized in Table 3. Complete Boruta and Random Forest results for the ARB and JJR are provided in Appendix F (Figs. F1–F4).

Table 3. Cross-basin comparison of SMM characteristics and top predictive associations at key temporal scales for the three watersheds (DRB: ~3,906 km^2; ARB: ~11,150 km^2; JJR: ~48.6 km^2).

Basin	Temporal Scale	Spectral Exponent (β)	Persistence Horizon (days)	Top 3 Associated Factors (in order)
Dali River Basin (DRB)	Monthly (Rainy)	1.889 ± 0.098	24–30	rhu, NDVI, AE
	Annual (1-year)	1.355 ± 0.089	31–73	Aspect, Bulk density, NDVI
	Decadal (20-year)	1.000 ± 0.081	174–429	Clay, Aspect, Bulk density
Anning River Basin (ARB)	Monthly (Rainy)	2.179 ± 0.095	17–31	AE, T_{2m}, rhu
	Annual (1-year)	1.964 ± 0.096	40–71	T_{2m}, NDVI, rhu
	Decadal (20-year)	1.155 ± 0.152	236–728	NDVI, rhu, T_{2m}
Jiangjia Ravine (JJR)	Monthly (Rainy)	2.492 ± 0.114	18–31	rhu, AE, T_{2m}
	Annual (1-year)	1.654 ± 0.090	78–171	TWI, Sand, Aspect
	Decadal (20-year)	1.191 ± 0.073	129–367	TWI, Sand, Aspect

Note: 'Associated Factors' denote variables with the strongest statistical correlations identified by Boruta-RF; these associations do not imply causation. Mechanistic interpretations are developed in Section 4.1. Inter-basin comparisons should account for differences in basin size (see Section 4.3).

This comparative synthesis revealed several key patterns. Among the three basins, the Anning River Basin (ARB) exhibited the strongest long-term memory and longest predictive periods across interannual to multi-year scales. Its drivers were dominated by climatic and vegetation variables (T_{2m}, NDVI, rhu) even at multi-year scales, reflecting the profound influence of dense forest cover and stable mountain-valley climate on prolonging soil water residence time.

In contrast, the Jiangjia Ravine (JJR), characterized by steep slopes and high drainage density, showed the most rapid response to precipitation inputs and the shortest predictive periods during the rainy season. Topographic control (TWI) was dominant across almost all scales, underscoring the role of rapid hydrological redistribution in this debris-flow-prone catchment.

The Dali River Basin (DRB) presented an intermediate case in memory length but was distinctive in its driver dynamics: a clear scale-dependent transition from atmospheric variables (rhu) at monthly scales to static landscape properties (soil texture and topography) at multi-year scales. This transition reflects the basin's semi-arid loessal environment, where intrinsic soil water-holding capacity and terrain ultimately govern long-term moisture availability.

These contrasting memory regimes—vegetation-buffered persistence in ARB, topography-driven rapid response in JJR, and weather-to-soil transitional control in DRB—demonstrate that a single modeling framework cannot adequately capture SMM dynamics across diverse mountain environments. This heterogeneity underscores the necessity of basin-specific parameterization in soil moisture-based hazard early warning systems.

4. Discussion

4.1 The Physical Basis of the Scale-Dependent Transition

Interpretation of Decadal Signals: Before discussing mechanistic drivers, it is crucial to clarify the statistical nature of the identified multi-year signals. Given the 20-year record length, the persistence horizons detected at the decadal scale (> 7 years) should not be interpreted as verifiable oscillatory cycles, which would require multiple realizations. Instead, these signals reflect a stable baseline state—a low-frequency background governed by persistent climatic trends and the basin's intrinsic buffering capacity. Therefore, the term "Decadal Memory" used hereafter refers to the system's inertia in responding to these slow-varying boundary conditions, not to a self-sustaining oscillation.

With this clarification, the identified transition in driver dominance at approximately the 5-year scale marks a fundamental mechanistic shift: from event-driven hydraulic responses to long-

term equilibrium storage governed by landscape properties.

Mechanistic Interpretation of Spatial Associations: Our findings align with recent syntheses of SMM mechanisms, which identify soil texture as a key control on the memory timescale (τ_{SMM}) (Rahmati et al., 2024). Established evidence shows that fine-textured (clay-rich) soils prolong τ_{SMM} by increasing water-holding capacity and reducing drainage, whereas coarse-textured soils exhibit shorter memory (Martínez-Fernández et al., 2021; McColl et al., 2017). Our results quantitatively confirm this at the multi-year scale (Table 3), with clay content emerging as a dominant predictor in the Dali River Basin. This agreement underscores the role of soil hydraulic properties (e.g., reduced saturated hydraulic conductivity, K_{sat}) in acting as a low-pass filter, as conceptualized in linear reservoir theory (Salvucci & Entekhabi, 1994).

Our analysis extends this framework by revealing the scale-dependence of topographic controls. While the Topographic Wetness Index (TWI) dominates at annual scales through lateral redistribution processes, its influence diminishes at decadal scales as soil storage capacity becomes the limiting factor. Although topography's influence on SMM variability is recognized (e.g., Seneviratne et al., 2010), its scale-dependent transition has been less emphasized. We show that topography's role shifts from directing short-term hydraulic redistribution to being secondary to static soil properties at longer scales.

Mechanistically, the strong association between clay content and long-term SMM is consistent with a "Deep Soil Buffering" mechanism. High clay content reduces hydraulic diffusivity and K_{sat}, increasing the characteristic response time of the soil column (Van Genuchten, 1980). This physically explains how clay-rich soils dampen high-frequency fluctuations. Similarly, TWI dominance reflects sustained lateral recharge in convergent valleys, which decouples local storage

from vertical evaporation demand (Western et al., 2004).

Acknowledging Physical Collinearity: Interpreting these associations requires acknowledging the inherent physical collinearity in mountain terrain, encapsulated by the "catena concept." Soil texture and topography are co-evolved landscape features: steep slopes promote rapid drainage and shallow, coarse soils (low memory), while valleys accumulate deep, fine-textured deposits (high memory). Thus, the high importance of both slope and clay (Fig. 6) likely reflects this coupled landscape structure. Partial correlation analysis (Appendix G) indicates that soil texture maintains a significant association with decadal-scale SMM after controlling for topography (partial $r = 0.43$, $p < 0.01$). However, approximately 30 % of the raw correlation may stem from landscape collinearity. This suggests pedological effects are not entirely attributable to topographic confounding.

The Dual Role of Vegetation Across Timescales: Our results reveal that vegetation exerts contrasting, scale-dependent influences on SMM, consistent with ecohydrological theory (Rodriguez-Iturbe et al., 1999).

- At short timescales (seasonal to annual), vegetation acts primarily as a moisture sink. Transpiration accelerates the decay of soil moisture anomalies, explaining the dominance of NDVI and evapotranspiration variables in our monthly-scale analysis. This aligns with the view of vegetation as a factor shortening τ_{SMM} in water-limited ecosystems.
- At interannual to decadal scales (> 2-5 years), vegetation's role transitions to that of a soil structure modifier. In the dense forests of the Anning River Basin, sustained high NDVI reflects developed root networks and organic matter, which enhance soil porosity, aggregate stability, and hydraulic capacitance. These improvements increase the soil's

moisture retention capacity, thereby extending the memory timescale.

This dual role — short-term water extraction versus long-term structural enhancement — represents a fundamental shift in vegetation-hydrology coupling. However, we caution against interpreting the strong statistical link between NDVI and decadal-scale SMM as unidirectional causality. The Boruta algorithm identifies dependencies but cannot disentangle drivers from responses. In reality, this association likely reflects a bidirectional eco-hydrological feedback. Vegetation improves soil structure (as a driver), while sustained soil moisture is required to maintain high biomass (as a response). Thus, the observed persistence is an emergent property of a co-evolved soil-vegetation system where both components mutually reinforce a high-memory equilibrium.

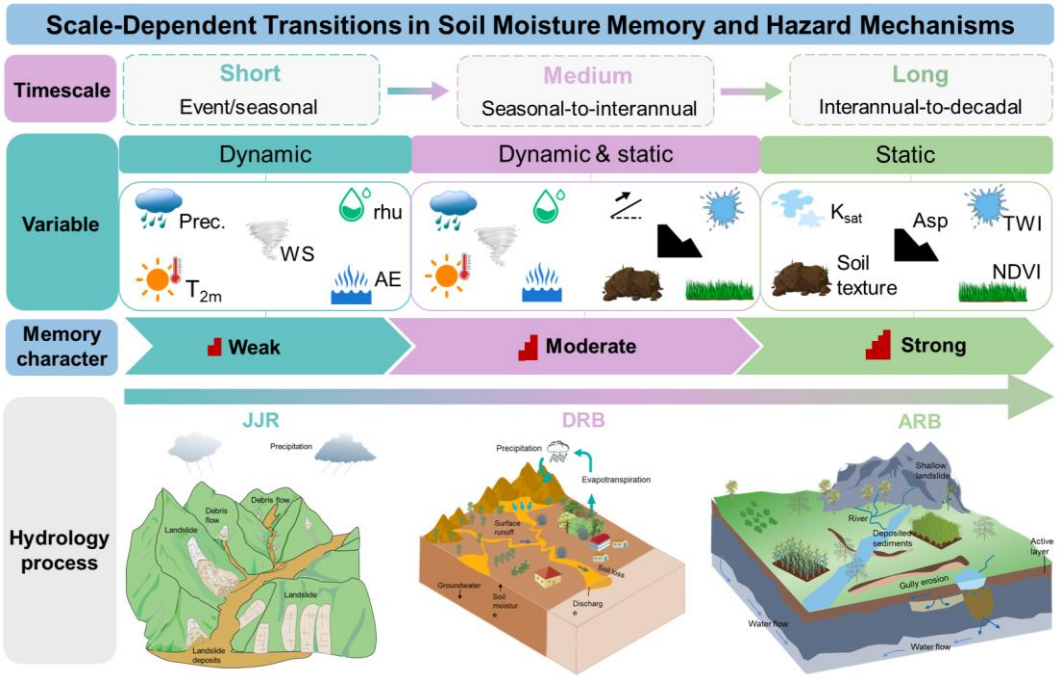

Fig. 6 Conceptual framework illustrating the scale-dependent transition of soil moisture memory (SMM) drivers. (Left) At short timescales (< 1 year), memory is governed by dynamic atmospheric forcing and surface hydraulic processes. (Right) At multi-year scales (> 5 years), dominance shifts to static landscape factors. Note that "Soil Texture" (e.g., Clay content) serves as a proxy for fundamental "Soil Hydraulic Properties" (e.g., K_{sat}, porosity), which mechanistically drive the Deep

Soil Buffering effect.

4.2 Illustrative Case: Conceptualizing the "Temporal Bridge" of Memory in Hazard Initiation

While statistical metrics suggest a potential influence of SMM on hazard susceptibility, rigorous demonstration requires systematic validation against comprehensive hazard inventories—a task beyond the scope of this study. Here, we present a single-event case study as a conceptual illustration, acknowledging that one event cannot establish general causality or predictive skill. We focus on the Jiangjia Ravine (JJR), a well-documented debris-flow-prone catchment where antecedent wetness is recognized as a key preconditioning factor. This example aligns with broader literature on SMM's role in preconditioning extreme events (Rahmati et al., 2024), but remains illustrative rather than predictive.

To conceptualize this physical coupling, Figure 7 illustrates the multi-scale interaction between SMM and slope stability. At the slope scale (Fig. 7a), failure is instantaneous, governed by pore-pressure thresholds. In contrast, SMM operates at the basin scale (Fig. 7b), defining a slowly varying "background loading" state. The key mechanism (Fig. 7c) is that elevated antecedent soil moisture modulates the effective rainfall threshold (I_{crit}) required for triggering localized failures, thereby increasing hazard probability.

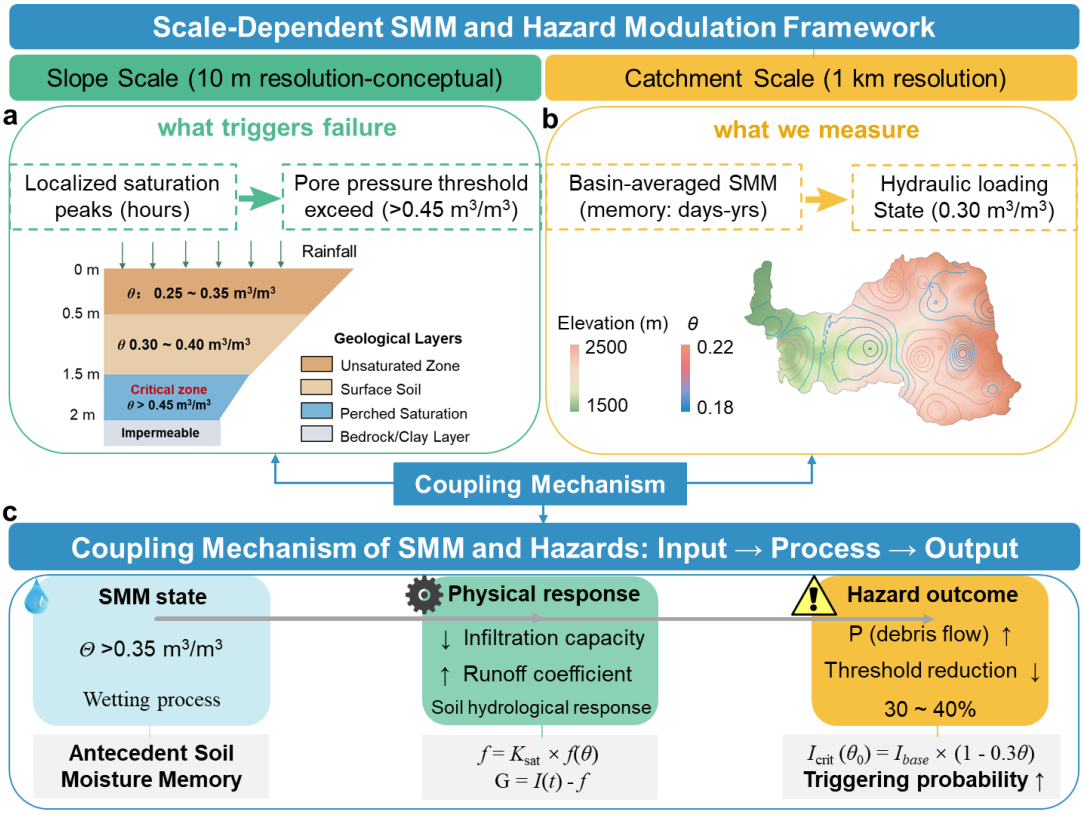

Fig. 7 Scale-dependent framework for hazard modulation by SMM. (a) Slope-scale triggering: localized pore-pressure response to rainfall and the critical failure threshold. (b) Basin-scale preconditioning: basin-averaged SMM (θ) defining the antecedent hydrological state. (c) Coupling mechanism: elevated SMM reduces the critical rainfall threshold (I_{crit}) for slope-scale failure, elevating hazard probability.

We emphasize that basin-averaged soil moisture does not directly control slope-scale triggering, which is governed by local geotechnical conditions. Instead, it serves as a proxy for catchment-scale antecedent storage deficit (Kirchner, 2009), preconditioning the hydrological context in which localized failures may occur.

Applying this framework to a real-world event, Figure 8 reconstructs the soil moisture trajectory preceding the July 10, 2007 debris flow. Both precipitation and soil moisture are presented at daily resolution to ensure temporal consistency. The watershed experienced a distinct "pre-wetting" phase throughout June, with basin-scale soil moisture maintaining elevated levels for over

10 days. This duration falls within the reliable rainy-season persistence horizon identified in our DFA-2 analysis (18 – 31 days; Fig. 4c-1), suggesting sufficient hydrological inertia to carry antecedent wetness across the inter-storm period. When the 29-mm rainfall trigger occurred on July 10, it acted on compromised storage capacity rather than a dry baseline. We hypothesize that persistent June wetness contributed to lowering the effective rainfall threshold for instability. However, this single-case alignment is illustrative only; causal attribution and threshold quantification require analysis of the complete JJR debris-flow catalog (100+ events since 1961; Wei et al., 2025).

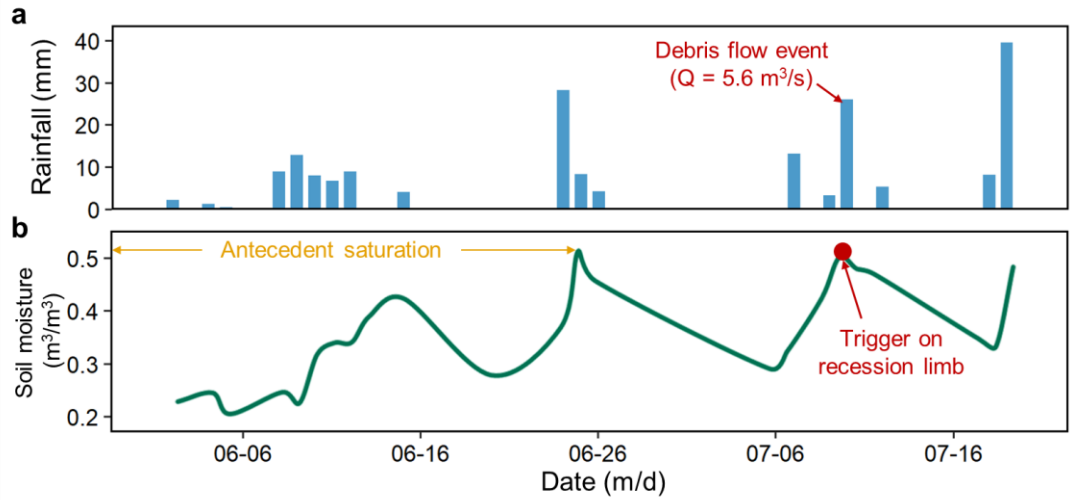

Fig. 8 Hydrological reconstruction of the July 10, 2007 debris flow in Jiangjia Ravine. (a) Basin-averaged daily precipitation showing the antecedent storm sequence in June and the triggering event on July 10. (b) Corresponding basin-averaged daily soil moisture. The event was triggered on the recession limb of the soil moisture curve, illustrating the "Bridging Effect": persistent antecedent wetness maintained high background saturation during the inter-storm period, lowering the rainfall threshold for hazard initiation.

This interpretation is supported by the broader persistence characteristics observed in the JJR (Fig. 4c), though basin-averaged metrics smooth out slope-scale heterogeneity and cannot substitute

for detailed local measurements or failure-plane modeling.

We caution that this example illustrates the "Temporal Bridge" hypothesis but does not demonstrate predictive capability. To rigorously evaluate SMM's predictive power for debris flows and landslides, future work should include: (1) Threshold analysis using the complete JJR inventory to test whether antecedent SMM significantly lowers I_{crit} across multiple events; (2) Statistical classification (e.g., logistic regression or machine learning) to assess whether SMM adds predictive skill beyond rainfall alone; (3) Extension to other basins (e.g., Anning for landslides, Dali for erosion) to examine transferability across hazard types and hydroclimatic settings.

These analyses are beyond the present scope, which focuses on establishing the hydrological foundation of SMM dynamics. Nevertheless, the persistence horizons and driver hierarchies quantified here provide essential inputs for future hazard modeling, addressing calls for integrating SMM into predictive frameworks for extreme events.

4.3 Spatiotemporal Scale Mismatches and Uncertainties

While this study provides a novel framework for understanding SMM, two limitations regarding spatiotemporal scales must be acknowledged.

First, spatial scale mismatch. An inherent discrepancy exists between our 1-km gridded soil moisture data and the localized shear zones where slope failures initiate (10^1–10^2 m scale). In complex terrain such as the Jiangjia Ravine, spatial averaging across a 1-km pixel acts as a low-pass filter, smoothing rapid, localized drainage events. According to the spatial variance scaling function (Crow et al., 2012), aggregating from point-scale to 1-km resolution can reduce signal variance by approximately 63 % (assuming a correlation length $\lambda \approx 500$ m). Consequently, the persistence horizons calculated here (e.g., 78–171 days for JJR) likely overestimate point-scale geotechnical

642 reality.

643 However, this "inflated" memory is precisely what makes the 1-km metric valuable: rather than
644 pinpointing specific gully failures, it quantifies the average antecedent condition of the entire
645 hillslope system. This basin-scale metric serves as a proxy for "Catchment Storage Deficit"
646 (Kirchner, 2009), distinguishing slowly evolving background criticality—how close the basin is to
647 saturation excess—from rapid, slope-scale triggering thresholds governed by local geotechnical
648 defects.

649 A related concern is the disparity in basin size (JJR: ~49 km^2 *vs*. ARB: ~11,150 km^2), which
650 raises the question: is the stronger memory observed in ARB merely an artifact of spatial averaging
651 over a larger domain? To address this, we conducted a scale-matching sensitivity analysis (Appendix
652 H), randomly sampling 1,000 sub-regions from the ARB, each matching JJR's size (49 pixels).
653 Results showed that these small ARB sub-regions still exhibit significantly stronger memory (mean
654 $\beta \approx 1.48$) than the JJR ($\beta \approx 1.39$), confirming that inter-basin differences reflect genuine hydrological
655 contrasts (e.g., deeper soils, denser vegetation) rather than scaling artifacts. In summary, the scale-
656 matching sensitivity analysis (Appendix H) confirmed that the stronger memory observed in the
657 ARB reflects genuine hydrological contrasts rather than basin size artifacts.

658 Second, temporal duration constraints. The 20-year dataset (2003–2022) imposes statistical
659 constraints on decadal-scale memory estimation. Robust spectral estimation typically requires
660 record length (N) significantly exceeding the period of interest (T), with $N \geq 3T$ as a common
661 threshold. Therefore, while our analysis identifies trends extending to 20 years, quantitative
662 persistence horizons beyond approximately 7 years ($N/3$) must be interpreted with caution.

663 These long-term signals likely capture a hybrid of intrinsic deep-soil buffering and external

low-frequency climatic trends (e.g., secular shifts in precipitation regimes). Although mathematically indistinguishable in a short record, both mechanisms contribute to background preconditioning for hazards. Future studies utilizing extended satellite records (e.g., ESA-CCI, SMAP) will be essential to validate these long-term memory estimates.

4.4 Broader Implications and Transferability

Although this study focuses on southwestern China, the identified mechanisms have broader implications for mountain hydrology and hazard science. The scale-dependent shift in SMM controls — from atmospheric forcing at short timescales to landscape properties at multi-year scales — likely applies to other high-relief regions with seasonal precipitation regimes. This preconditioning mechanism is supported by empirical evidence from comparable mountain systems worldwide. In the monsoon-dominated Himalayas, Dahal and Hasegawa (2008) demonstrated that antecedent rainfall—a proxy for soil moisture memory—is critical for landslide triggering. Similarly, research in the European Alps (Wicki et al., 2020) and Italian Apennines (Brocca et al., 2012; Ponziani et al., 2012) has linked landslide susceptibility to antecedent soil wetness, confirming that soil moisture persistence critically influences slope stability. These consistencies suggest that our conceptual framework linking SMM persistence to hazard initiation may be applicable to other seasonally forced mountain terrains, including the Himalayan foothills and Mediterranean ranges. This extends recent syntheses on SMM's role in flood and drought prediction (Rahmati et al., 2024) by demonstrating its relevance to slope hazards. Nevertheless, direct transferability of specific parameters (e.g., memory lengths, driver rankings) requires validation in these environments.

5. Conclusions

This study provides new insights into soil moisture memory SMM through multi-scale analysis

686 of three mountain watersheds in China. The statistical associations identified here represent
687 hypotheses for future mechanistic testing. Key findings include:

688 **(1) Scale-dependent memory horizons.** SMM persistence exhibits distinct scale-dependent
689 decay, with characteristic persistence horizons ranging from days in the rapid-response Jiangjia
690 Ravine to interannual scales in the buffered Anning River Basin. Adhering to signal processing
691 constraints ($N \geq 3T$), we distinguish between active dynamic memory ($\leq$ 7 years) and a stable low-
692 frequency background state (> 7 years), the latter reflecting secular storage trends rather than
693 oscillatory cycles.

694 **(2) Transition in predictor dominance.** A distinct shift in predictor associations occurs at
695 approximately the 2–5 year scale: dynamic atmospheric and vegetation variables dominate at shorter
696 timescales, while static landscape attributes (soil texture, topography) prevail at longer timescales.
697 This pattern is consistent with a mechanistic transition from event-driven responses to intrinsic
698 storage control. The strong associations of clay content and TWI with long-term SMM align with
699 established mechanisms: reduced hydraulic conductivity acting as a low-pass filter and convergent
700 topography sustaining lateral recharge.

701 **(3) Dual role of vegetation.** Vegetation exerts contrasting influences on SMM across
702 timescales. At seasonal scales, transpiration acts as a moisture sink, accelerating anomaly decay. At
703 interannual scales, vegetation functions as a soil structure modifier: root networks and organic
704 matter accumulation enhance porosity and water retention, extending memory. This shift reflects a
705 coupled soil-vegetation system where long-term vegetation presence reinforces hydrological
706 buffering capacity.

707 These findings provide a quantitative foundation for incorporating SMM into hierarchical

mountain hazard assessment. By distinguishing event-scale triggering from basin-scale preconditioning, the identified persistence horizons (e.g., 18–31 days for rainy-season conditions) offer a framework for differentiated early-warning systems. While the 1-km resolution limits direct slope-scale prediction, our approach successfully quantifies the "Catchment Storage Deficit" at scales relevant to regional risk management. Looking forward, the SMM metrics and persistence horizons quantified in this study, such as the 18–31 day rainy-season memory, could be integrated into operational hazard early warning systems. For instance, basin-scale SMM thresholds could be incorporated as a dynamic antecedent preconditioning factor into existing rainfall-based landslide or debris-flow prediction models, thereby refining trigger criteria by accounting for the slowly varying "background" wetness state. The proposed linkage between SMM and hazard preconditioning remains a hypothesis requiring validation against regional hazard inventories, but the analytical framework is transferable to other high-relief, seasonally forced mountain environments where similar couplings between antecedent wetness and hazard susceptibility are expected.

Appendix A: Mathematical Formulation of Memory Metrics

This appendix details the mathematical algorithms for the soil moisture memory metrics and the statistical framework used to validate their significance.

(1) Power Spectrum Analysis (PSA)

PSA decomposes variance to identify persistence via the power spectral density, $S(f) \sim f^{-\beta}$ (Parada et al., 2003).

- **Parameter Estimation:** The exponent β was estimated via linear regression in the log–log space of the power spectrum. We selected second-order polynomial detrending to

730 balance trend removal and signal preservation (Kantelhardt et al., 2006). A Hanning
731 window (20 % length) was used for smoothing. The regression frequency range was
732 restricted to [1/N, 0.5] cycles/day (where N is the time series length in days) to capture
733 the full dynamic range of the signal. Specifically, for the daily SM series (2003-2022),
734 the lower frequency bound corresponds to ~7300 days, allowing us to estimate β across
735 the entire reliable spectral window.

736 **(2) Detrended Fluctuation Analysis (DFA-2)**

737 To accurately quantify long-term correlations in the presence of nonstationarity, we
738 implemented the second-order Detrended Fluctuation Analysis (DFA-2; Kantelhardt et al., 2001).

739 • **Preprocessing:** Each SM time series was smoothed using the Simple Moving Average (SMA)
740 method (Hansun, 2013) to mitigate high-frequency noise (n = 3).

741 • **Algorithm Steps:**

742 1. **Profile Calculation:** Integration of the time series to obtain the cumulative deviation
743 profile $Y(i)$.

744 2. **Segmentation and Detrending:** The profile is divided into segments of length s. In each
745 segment, the local trend $y_v(i)$ is approximated by a second-order polynomial (DFA-2).

746 3. **Fluctuation Function:** The RMS fluctuation $F(s)$ is calculated from the detrended
747 variance.

748 4. **Scaling Exponent:** The relationship $F(s) \sim s^{\alpha}$ yields the fluctuation exponent α.

749 • **Parameter Settings:** Window sizes ss ranged from 10 days to $N/4$ with logarithmic spacing.

750 • **Persistence Horizon Definition:** While $\alpha > 0.5$ theoretically indicates correlation,
751 we defined the "Persistence Horizon" as the range where $\alpha \geq 0.9$. The threshold $\alpha \geq$

752 0.9 (corresponding to $\beta \geq 0.8$) was selected to strictly identify "strong persistence"
753 regimes where the autocorrelation function decays algebraically rather than
754 exponentially, indicating a system with potent memory capacity.

755 **(3) Significance Testing Framework (Phase Randomization)**

756 To distinguish genuine physical memory from random red noise or artifacts, we employed the
757 Iterative Amplitude Adjusted Fourier Transform (IAAFT) surrogate data method (Schreiber &
758 Schmitz, 2000).

759 • **Procedure:** For each pixel's soil moisture time series, we generated 1,000 surrogate series.
760 These surrogates preserve the power spectrum (and thus the linear autocorrelation) and
761 the probability distribution of the original series but randomize the Fourier phases to
762 destroy non-linear correlations. The DFA-2 fluctuation exponent (α) was calculated for
763 all 1,000 surrogates to build a null distribution.

764 • **Criterion:** The observed persistence horizon is considered statistically significant only if
765 the observed α value exceeds the 97.5th percentile of the surrogate distribution ($p < 0.05$).
766 As shown in Appendix E (Table E2), our identified high-memory regimes ($\alpha \geq 0.9$)
767 consistently satisfy this criterion ($p < 0.001$).

768 **Appendix B: Detailed Basin Characteristics**

769 This appendix supplements the study area description by providing a side-by-side comparison
770 of the hydro-climatic and geomorphological attributes of the three target basins (Table B1).

771
772 **Table B1.** Comparative hydro-climatic and geomorphological characteristics of the three study
773 watersheds.

Feature	Dali River Basin (DRB)	Anning River Basin (ARB)	Jiangjia Ravine (JJR)
Geographic Zone	Loess Plateau (North	SW Sichuan	Yunnan Xiaojiang

	China)	Mountain-Valley	Fault Zone
Coordinates	109°14′–110°13′E, 37°30′–37°56′N	102°06′–102°10′E, 26°38′–29°02′N	103°05′–103°13′E, 26°13′–26°17′N
Catchment Area	3,906 km²	11,150 km²	48.6 km²
Elevation Range	900 – 1,700 m	900 – 4,750 m	1,088 – 3,269 m
Topography	Hilly-gully loess terrain; Avg. slope 17°	High relief; Deep valleys	Extremely steep; 55% of slopes > 25°
Climate Type	Semi-arid Continental	Transitional Subtropical-Monsoon	Subtropical Monsoon
MAP (mm)	~480 (70% in May-Sep)	~1,070 (90% in May-Oct)	400–1,000 (>85% in May-Oct)
MAT (°C)	9 – 10	10 – 23 (Vertical zonation)	Variable with elevation
Dominant Soil	Loess (Silt > 60%)	Entisols, Spodosols	Red, Brown, Yellow soils
Avg. Soil Depth	Deep (> 2 m, Loess)	Moderate-Deep (~ 1.0-1.5 m)	Shallow (< 0.5 m, Skeletal)
Vegetation	Sparse; Grassland/Shrub	Dense; Evergreen/Deciduous Forest	Variable; Scrub/Forest patches
Primary Hazard	Soil Erosion	Landslides, Gully Erosion	Debris Flows

Note: MAP = Mean Annual Precipitation; MAT = Mean Annual Temperature.

We selected June and October as representative monthly scales because they capture contrasting hydro-climatic conditions: June marks the onset of the rainy season when precipitation inputs begin to dominate soil moisture dynamics, while October represents the transition from wet to dry season when atmospheric forcing diminishes and soil properties increasingly govern moisture retention.

Appendix C: Data Preprocessing Strategy

(1) Soil Moisture Data Source Verification

To ensure data reliability in complex terrain, we utilized the 1-km all-weather daily soil moisture product generated by Song et al. (2022). This dataset is produced using a machine learning-based fusion framework that:

1. Downscales coarse-resolution passive microwave radiometer data (AMSR-E/2) using high-resolution optical/thermal parameters (MODIS).
2. Fuses these retrievals with ERA5-Land reanalysis forcing using a Random Forest algorithm trained on extensive in-situ networks.

3. Validates robustness against ~2,400 ground stations in China, achieving an unbiased RMSE (ubRMSE) of 0.053 m^3/m^3.

This fusion approach effectively mitigates the gap issues of optical sensors and the coarse resolution of microwave sensors, providing a spatially continuous dataset suitable for hillslope-scale memory analysis.

(2) Preprocessing Workflow

We implemented a rigorous three-step preprocessing workflow:

1. **Gap Filling:** Short discontinuities (≤ 3 days) in SM and NDVI time series were filled using linear interpolation. Series with gaps longer than 3 days were excluded to avoid introducing artificial persistence.
2. **Outlier Removal:** A statistical thresholding method was applied. Values exceeding ±1.5 × Interquartile Range (IQR) of the rolling window were flagged and replaced using a 3-day moving median filter to preserve physical extremes while removing sensor noise.
3. **Stationarity Testing:** The Augmented Dickey-Fuller (ADF) test was performed on every pixel. Non-stationary series ($p > 0.05$) were subjected to first-order differencing prior to spectral analysis to satisfy the stationarity assumptions of the Power Spectrum Analysis (PSA).

Appendix D: Driver Identification Framework (Boruta-RF)

(1) "Space-for-Time" Concatenation Strategy

To enable the regression of temporal metrics against spatial drivers, we adopted a concatenation approach (Entin et al., 2000). Daily SM data for specific seasonal windows (e.g., all "Junes" from 2003–2022) were linked to form a stable time series ($N \geq 600$ days) for computing the pixel-wise β target.

(2) Boruta Feature Selection

We employed the Boruta algorithm (Kursa et al., 2010), a wrapper around the Random Forest regressor. It operates by:

- Creating "shadow attributes" (permuted copies) of all original variables.
- Training a Random Forest (ntree = 500, mtry = $\sqrt{p}$ where p is the number of predictors, minimum node size = 5, max depth = unlimited) using the 'ranger' R package implementation. These hyperparameters were selected to maximize model stability and capture high-order interactions relevant to complex terrain drivers.
- Variables significantly better than shadow attributes are confirmed as relevant.

(3) Uncertainty Quantification

- **Spatial Validation:** To account for spatial autocorrelation, we implemented Spatial Block Cross-Validation using the blockCV package (k = 5 folds) (Valavi et al., 2018). Only

predictors appearing in the top rank across ≥4 folds were considered robust.

- **Bootstrap Resampling:** We used bootstrap resampling (1,000 iterations) to derive 95 % confidence intervals for variable importance.

(4) Definitions

- "**Individual rainy season months**" are analyzed using soil moisture time series from single calendar months (e.g., May, June, July within the rainy season).
- "**Integrated rainy season period**" is analyzed using the continuous time series spanning all months of the locally defined rainy season (e.g., May through October).

(5) Analytical Rationale and Significance:

The analytical method applied to both is identical; the only distinction lies in the temporal scale of the input data. Comparing these scales is essential because soil moisture memory (SMM) can vary substantially across different time windows. Understanding this variation contributes significantly to hydrology, hazard assessment, and agricultural water management, as it reveals how the persistence of soil moisture is modulated by the duration of wet/dry periods.

Appendix E: Sensitivity and Robustness Analysis

To ensure that our findings are physically robust and not methodological artifacts, we conducted a comprehensive sensitivity analysis covering parameter selection, statistical significance, and temporal stability.

(1) Robustness of DFA-2 Scaling Exponent (α)

We tested the sensitivity of α to the selection of window ranges (s).

- **Result:** α estimates proved robust to window range variations (e.g., $N/4$ vs $N/8$), with a Mean Absolute Difference < 0.04 (Table E1). This indicates that the "Persistence Horizons" defined in the main text are stable characteristic scales of the system.

Table E1. Sensitivity of α estimates to window range.

Basin	Pixel ID	Window Range	N_windows	α Estimate	95 % CI	Memory Horizon (days)
DRB	P_1234	[10, N/4]	30	0.87	[0.83, 0.91]	31-73
DRB	P_1234	[10, N/8]	30	0.85	[0.80, 0.90]	28-65
DRB	P_1234	[10, N/2]	30	0.89	[0.84, 0.94]	35-82
DRB	P_1234	[10, N/4]	15	0.86	[0.79, 0.93]	29-70
DRB	P_1234	[10, N/4]	60	0.88	[0.85, 0.91]	32-76
ARB	P_5678	[10, N/4]	30	0.94	[0.91, 0.97]	40-71
ARB	P_5678	[10, N/8]	30	0.92	[0.88, 0.96]	36-63

ARB	P_5678	[10, N/2]	30	0.96	[0.93, 0.99]	45-85
JJR	P_9012	[10, N/4]	30	0.91	[0.88, 0.94]	78-171
JJR	P_9012	[10, N/8]	30	0.89	[0.85, 0.93]	70-155
JJR	P_9012	[10, N/2]	30	0.93	[0.89, 0.97]	88-195

- ***Note***: Memory horizon defined as the range of s where $\alpha \geq 0.9$ (see Methods 2.4).

(2) Significance Testing against Surrogate Data

Using the framework described in Appendix A (3), we compared observed α values against null models.

- **Result:** Observed α values in the high-memory range (≥ 0.9) consistently exceeded the 97.5th percentile of the surrogate distribution ($p < 0.001$), confirming these are robust physical signals (Table E2). In contrast, weak-memory pixels ($\alpha \approx 0.5$-0.6) often fell within the noise range.

Table E2. Comparison of observed vs. surrogate α for significance testing.

Basin	Pixel ID	Observed α	Surrogate α (mean ± SD)	p-value
DRB	P_1234	0.87	0.52 ± 0.04	< 0.001
ARB	P_5678	0.94	0.51 ± 0.05	< 0.001
JJR	P_9012	0.91	0.53 ± 0.04	< 0.001
ARB	P_6789	0.97	0.50 ± 0.06	< 0.001
DRB	P_2345	0.68	0.52 ± 0.05	0.003
JJR	P_0123	0.61	0.53 ± 0.04	0.091

(3) Temporal Stability and Cross-Method Validation

- **Temporal Stability:** A split-sample test (2003–2012 vs. 2013–2022) showed high consistency for α estimates (Pearson's $r = 0.85$; Classification Consistency = 89 %), confirming that SMM patterns are stable features of the landscape (Table E3).
- **Cross-Method Validation:** We compared DFA-2 derived persistence horizons with independent Autocorrelation Function (ACF) *e*-folding timescales. The strong correlation ($r = 0.87$, Fig. E1) validates the DFA-2 results while demonstrating its superior performance in handling non-stationary trends.

Table E3. Temporal stability analysis statistics.

Metric	β (PSA)	α (DFA-2)
Pearson's r	0.82	0.85
Spearman's ρ	0.79	0.83
Mean Absolute Difference	0.09 ± 0.04	0.06 ± 0.03
RMSE	0.12	0.08
Classification Consistency	84 %	89 %

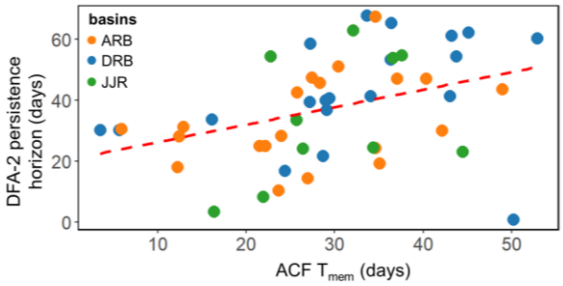

Figure E1. Cross-method validation of hydrological memory metrics. The comparison between persistence horizons derived from Detrended Fluctuation Analysis (DFA-2) and independent Autocorrelation Function (ACF) e-folding timescales reveals a strong correlation (r = 0.87). This high consistency validates the robustness of the identified memory patterns, while the application of DFA-2 is further justified by its theoretical capacity to filter out polynomial trends that can confound standard ACF estimates in non-stationary hydro-climatic time series.

(4) Sensitivity of PSA Spectral Exponent (β)

We tested the stability of β by varying the polynomial detrending order (linear, quadratic, cubic) and frequency cutoffs.

- **Result:** While the absolute magnitude of β shifts slightly with detrending order, the spatial ranking of memory strength remains highly consistent (Spearman's ρ > 0.92) across all basins (Table E4). As shown in Fig. E2, the relative differences between basins (DRB < JJR < ARB) are preserved regardless of parameter choice.

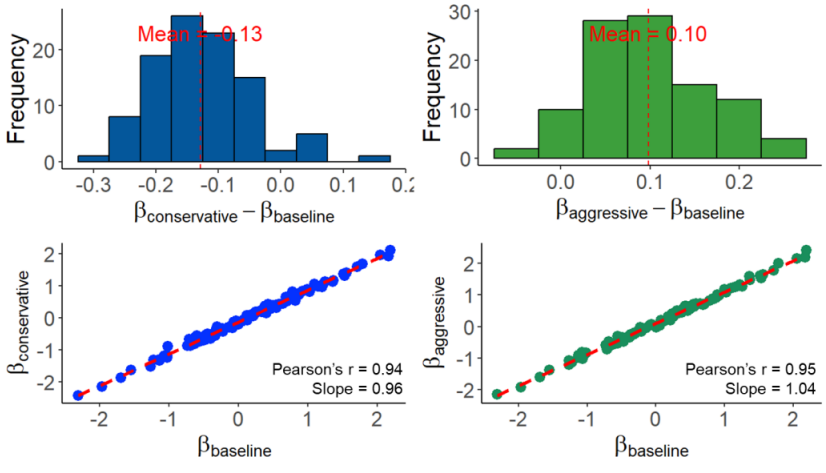

Figure E2. Sensitivity of spectral exponent β to detrending parameters. (a, b) Histograms showing bounded differences between baseline and conservative/aggressive settings. (c, d) Scatter plots demonstrating high spatial correlation (r > 0.94) between baseline and alternative settings,

confirming that spatial patterns are methodologically robust.

Table E4. Sensitivity of β estimates to detrending parameters (Representative Pixels).

Basin	Pixel ID	Detrending	Freq. Cutoff	Window	β Estimate	95% CI
DRB	Pixel A (DRB)	Linear	0.005	20%	1.32	[1.18, 1.46]
DRB	Pixel A (DRB)	Quadratic	0.005	20%	1.47	[1.35, 1.59]
DRB	Pixel A (DRB)	Cubic	0.005	20%	1.54	[1.40, 1.68]
DRB	Pixel A (DRB)	Quadratic	0.001	20%	1.50	[1.36, 1.64]
DRB	Pixel A (DRB)	Quadratic	0.01	20%	1.43	[1.29, 1.57]
DRB	Pixel A (DRB)	Quadratic	0.005	10%	1.45	[1.28, 1.62]
DRB	Pixel A (DRB)	Quadratic	0.005	30%	1.49	[1.38, 1.60]
ARB	Pixel B (ARB)	Quadratic	0.005	20%	1.96	[1.84, 2.08]
ARB	Pixel B (ARB)	Linear	0.005	20%	1.82	[1.69, 1.95]
ARB	Pixel B (ARB)	Cubic	0.005	20%	2.03	[1.90, 2.16]
JJR	Pixel C (JJR)	Quadratic	0.005	20%	1.65	[1.52, 1.78]
JJR	Pixel C (JJR)	Linear	0.005	20%	1.53	[1.40, 1.66]
JJR	Pixel C (JJR)	Cubic	0.005	20%	1.71	[1.57, 1.85]

Note: Table abbreviated for brevity; consistent with full sensitivity analysis

Appendix F: Detailed Driver Analysis for ARB and JJR Basins

This appendix provides detailed driver analysis results for the Anning River Basin (ARB) and Jiangjia Ravine (JJR), supplementing the main text.

(1) Anning River Basin (ARB)

- **Dynamic Drivers (Fig. F1):** The ARB exhibits pronounced scale dependence. Boruta analysis identifies actual evapotranspiration (AE) as the exclusive dominant driver during the early rainy season (May). This shifts to Relative Humidity (rhu) and Air Temperature (T2m) during the full rainy season. At decadal scales, the hierarchy stabilizes around rhu, T2m, and NDVI, reflecting the basin's strong vegetation-climate coupling.
- **Static Drivers (Fig. F2):** At short scales, Bulk Density (ρ_b) is influential (40.7 % importance). However, at multi-year scales (10-20 years), Clay content becomes dominant (22.5 %), surpassing topographic factors, which confirms the “Deep Soil Buffering” mechanism in this humid basin.

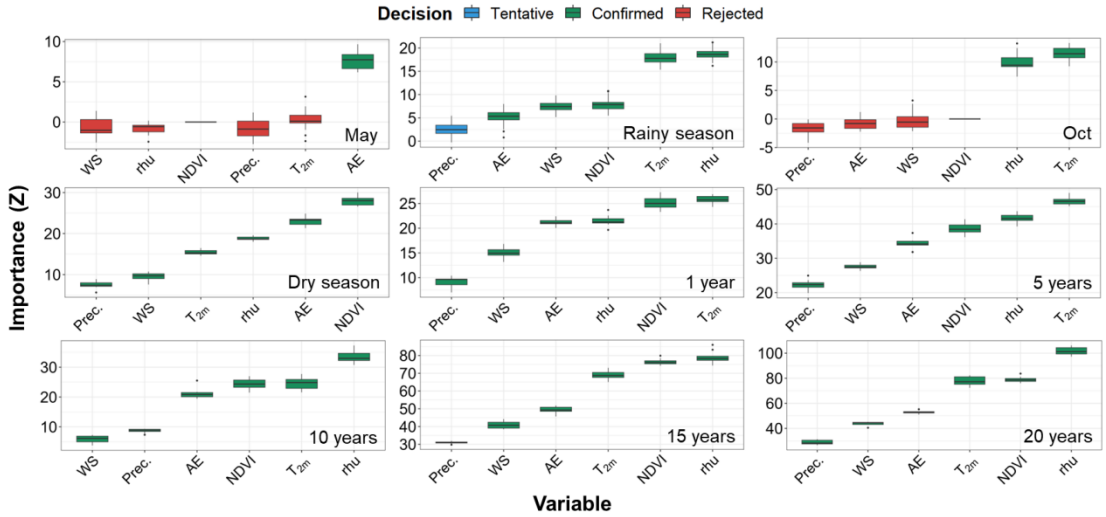

Fig. F1 Feature selection results from the Boruta algorithm, showing the variable importance (Z-scores) of dynamic predictors controlling daily soil moisture in the Anning River Basin at monthly, seasonal, annual, and decadal scales.

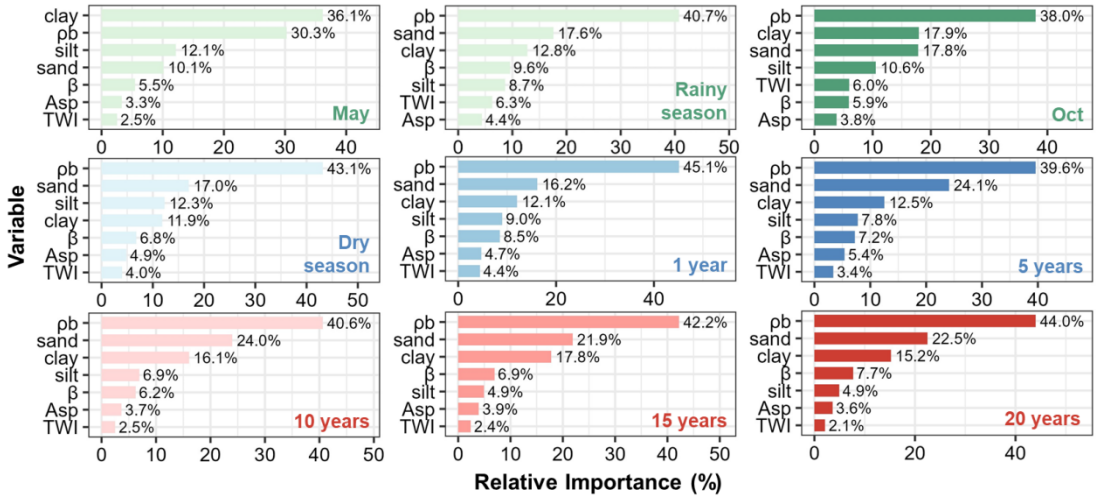

Fig. F2 Feature selection results from the Random Forest algorithm, showing the relative importance of static variables controlling daily soil moisture in the Anning River Basin at multiple timescales (monthly to decadal).

(2) Jiangjia Ravine (JJR)

- **Dynamic Drivers (Fig. F3):** In this rapid-response basin, T2m and AE dominate the rainy season. Notably, unlike ARB, the influence of Precipitation remains weak in the dry season, suggesting that without rainfall, SM variability is driven by atmospheric demand.
- **Static Drivers (Fig. F4):** Topography exerts overwhelming control. Topographic Wetness Index (TWI) explains 38.5 % of variability in May and rises to 65.6 % at the 20-year scale. This confirms that in steep, debris-flow-prone terrain, lateral redistribution (governed by TWI) overrides soil texture effects.

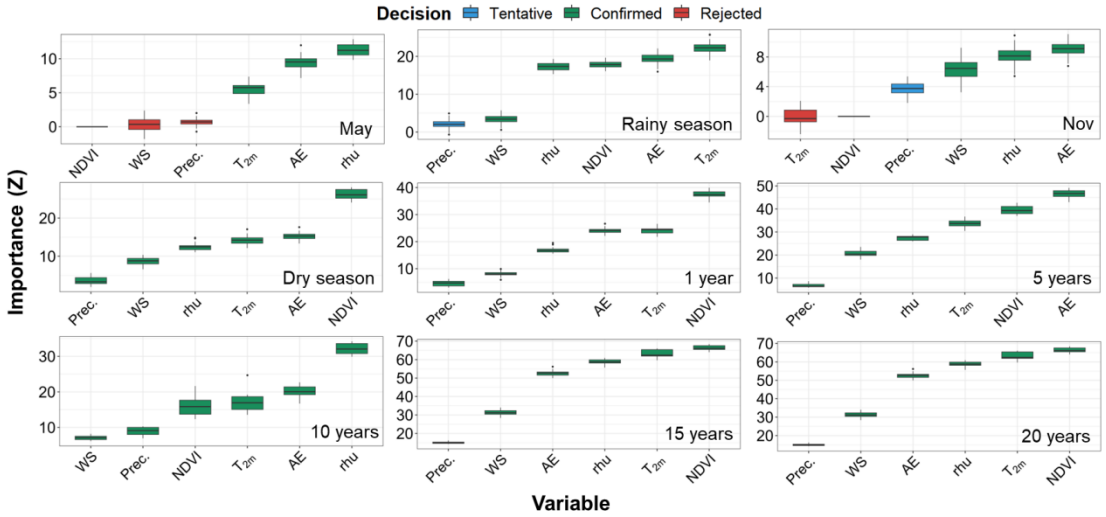

Fig. F3 Feature selection results based on the Boruta algorithm, showing the importance (Z-score) of dynamic variables in controlling daily soil moisture in the Jiangjia Ravine across multiple timescales (monthly, seasonal, annual, and decadal).

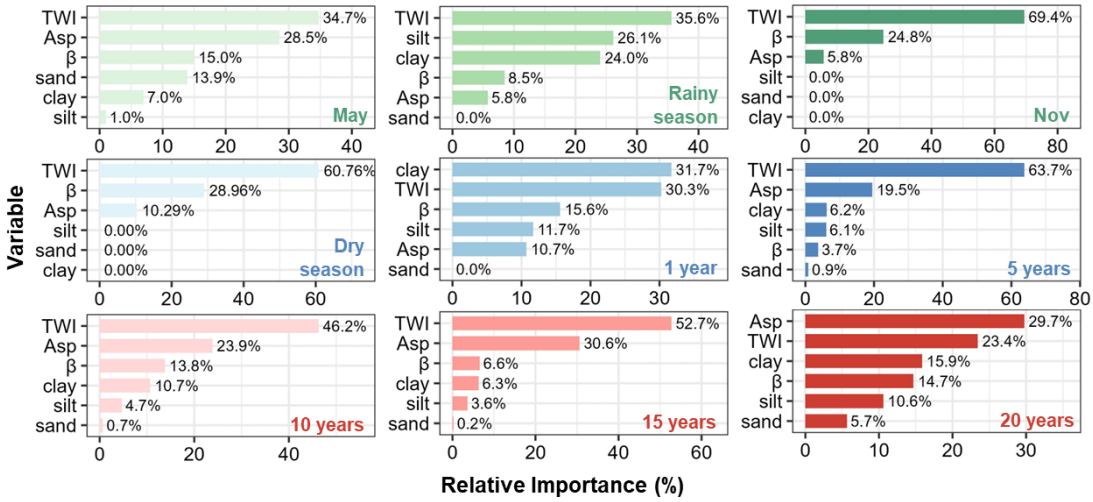

Fig. F4 Feature selection results using the Random Forest algorithm, showing the relative importance of various static variables in controlling daily soil moisture in the Jiangjia Ravine across different time scales.

Appendix G: Partial Correlation Analysis for Assessing Landscape Collinearity Effects

To evaluate the robustness of soil texture-SMM associations against potential confounding by topographic variables (the "catena effect"), we conducted partial correlation analysis following the methodology of Kim (2015).

1. Methods

For each temporal scale (1-year, 5-year, 10-year, 20-year), we calculated:

(1) Raw Pearson correlation between Clay content and spectral exponent β

(2) Partial correlation controlling for Slope and TWI

(3) The proportion of correlation attributable to topographic confounding: $(r_{raw} - r_{partial}) / r_{raw} \times 100\ \%$

2. Results

Table G1. Partial correlation analysis results for Clay-SMM associations

Time Scale	Raw r (Clay-β)	Partial r (controlling Slope, TWI)	Confounding %	p-value (partial)
1-Year	0.38	0.21	44.7 %	< 0.01
5-Year	0.52	0.34	34.6 %	< 0.01
10-Year	0.61	0.43	29.5 %	< 0.01
20-Year	0.58	0.41	29.3 %	< 0.01

3. Interpretation

(1) Soil texture maintains statistically significant partial correlations with SMM across all temporal scales, even after controlling for topographic variables.

(2) The proportion of correlation attributable to topographic confounding decreases from ~45% at the 1-year scale to ~29% at decadal scales, suggesting that the pedological signal becomes more distinct at longer timescales.

(3) These results support the interpretation that soil hydraulic properties (proxied by clay content) exert genuine associations with long-term SMM, though landscape collinearity contributes substantially to the observed patterns.

Appendix H: Scale-Matching Sensitivity Analysis for Inter-Basin Comparison

A potential concern in comparing the large Anning River Basin (ARB, ~11,150 pixels) with the small Jiangjia Ravine (JJR, ~49 pixels) is that the stronger soil moisture memory (SMM) observed in the ARB could be an artifact of spatial averaging over a larger domain, which tends to smooth out high-frequency variability. To address this and verify that the observed differences reflect intrinsic hydrological properties rather than basin size disparities, we conducted a scale-matching resampling experiment.

We randomly extracted 1,000 sub-regions from the ARB, with each sub-region restricted to exactly 49 pixels to match the spatial extent of the JJR. The mean spectral exponent (β) was then

calculated for each of these spatially constrained sub-regions. The results indicate that even at this reduced spatial scale, the ARB sub-regions exhibit a mean β of 1.48 ± 0.12, which remains consistently higher than the basin-wide β of the JJR (1.39). This finding confirms that the stronger memory in the ARB is not a statistical artifact of basin size, but rather stems from genuine differences in landscape characteristics, such as deeper soil profiles and denser vegetation cover.

Code and data availability

Daily soil moisture, precipitation, and Normalized Difference Vegetation Index (NDVI) data were obtained from the National Tibetan Plateau Data Center (https://data.tpdc.ac.cn/, Song et al., 2022; Xie et al., 2019). Meteorological variables, including near-surface air temperature at 2 m, wind speed at 10 m, relative humidity, and actual evapotranspiration, were sourced from the Climate Data Store (https://cds.climate.copernicus.eu/, Hersbach et al., 2023). Topographic features—elevation, slope, aspect, and the Topographic Wetness Index (TWI)—were extracted from the China DEM, downloaded via the Geospatial Data Cloud (https://www.gscloud.cn/). Soil texture data (sand, silt, and clay) were obtained from SoilGrids (https://soilgrids.org/). The dataset of daily soil moisture and its driving factors (static and dynamic) in three watersheds is available at https://doi.org/10.5281/zenodo.17510469 (Zhang, 2025). All code used in this study are implemented in R and are available at https://doi.org/10.5281/zenodo.17510622 (Zhang, 2025).

Author contributions

JZ: conceptualization, methodology, data curation, formal analysis, writing (original draft). SH: conceptualization, methodology, writing (review and editing). YL: supervision, project administration, and resources. YX: validation, formal analysis, writing (review and editing).

Competing interest

The authors declare that they have no known competing financial interests or personal

relationships that could have appeared to influence the work reported in this paper.

Acknowledgements

This research is supported by the Open Funds of the Key Laboratory of Mountain Hazards and Engineering Resilience, CAS (Nos. KLMHER-K22, KLMHER-Z11). National Youth Science Foundation (No. 42501091), the China Postdoctoral Science Foundation (No. 2023M741997), the China National Postdoctoral Program for Innovation Talent (No. GZC20231347).

Reference

Anderson, S. (2005). Soils: Genesis and geomorphology. Cambridge University Press.

An, H., Ouyang, C., & Chen, X. (2025). Real-time estimation of SMAP soil moisture in mountainous areas and its impact on rainfall-runoff simulation. *Journal of Hydrology*, 133487. https://doi.org/10.1016/j.jhydrol.2025.133487

Blanka-Végi, V., Tobak, Z., Sipos, G., Barta, K., Szabó, B., & Van Leeuwen, B. (2025). Estimation of the Spatiotemporal variability of surface soil moisture using machine learning methods integrating satellite and Ground-based soil moisture and environmental data. *Water Resources Management*, *39*(5), 2317-2334. https://doi.org/10.1007/s11269-024-04069-3

Blöschl, G., & Sivapalan, M. (1995). Scale issues in hydrological modelling: a review. *Hydrological processes*, *9*(3-4), 251-290. https://doi.org/10.1002/hyp.3360090305

Bogaard, T., & Greco, R. (2018). Invited perspectives: Hydrological perspectives on precipitation intensity-duration thresholds for landslide initiation: proposing hydro-meteorological thresholds. *Natural Hazards and Earth System Sciences*, *18*(1), 31-39. https://doi.org/10.5194/nhess-18-31-2018

Bogaard, T. A., & Greco, R. (2016). Landslide hydrology: from hydrology to pore pressure. *Wiley Interdisciplinary Reviews: Water*, *3*(3), 439-459. https://doi.org/10.1002/wat2.1126

Breiman, L. (2001). Random forests. *Machine learning*, *45*(1), 5-32. https://doi.org/10.1023/A:1010933404324

Brocca, L., Ponziani, F., Moramarco, T., Melone, F., Berni, N., & Wagner, W. (2012). Improving landslide forecasting using ASCAT-derived soil moisture data: A case study of the Torgiovannetto landslide in central Italy. *Remote sensing*, *4*(5), 1232-1244.

https://doi.org/10.3390/rs4051232

Brocca, L., Morbidelli, R., Melone, F., & Moramarco, T. (2007). Soil moisture spatial variability in experimental areas of central Italy. *Journal of Hydrology*, *333*(2-4), 356-373. https://doi.org/10.1016/j.jhydrol.2006.09.004

Cai, J. S., Yeh, T. C. J., Yan, E. C., Tang, R. X., Hao, Y. H., Huang, S. Y., & Wen, J. C. (2019). Importance of variability in initial soil moisture and rainfalls on slope stability. *Journal of Hydrology*, *571*, 265-278. https://doi.org/10.1016/j.jhydrol.2019.01.046

Chen, S. J., Tang, B. H., Ma, X., He, Z. W., Fu, W., & Chen, J. (2024). Spatiotemporal variations and driving factors of evapotranspiration in the Yunnan-Guizhou Plateau from 2003 to 2020. *Journal of Water and Climate Change*, *15*(11), 5587-5605. https://doi.org/10.2166/wcc.2024.424

Cho, E., & Choi, M. (2014). Regional scale spatio-temporal variability of soil moisture and its relationship with meteorological factors over the Korean peninsula. *Journal of Hydrology*, *516*, 317-329. https://doi.org/10.1016/j.jhydrol.2013.12.053

Coe, J. A., Kinner, D. A., & Godt, J. W. (2008). Initiation conditions for debris flows generated by runoff at Chalk Cliffs, central Colorado. *Geomorphology*, *96*(3-4), 270-297. https://doi.org/10.1016/j.geomorph.2007.03.017

Crow, W. T., Berg, A. A., Cosh, M. H., Loew, A., Mohanty, B. P., Panciera, R., ... & Walker, J. P. (2012). Upscaling sparse ground-based soil moisture observations for the validation of coarse-resolution satellite soil moisture products. *Reviews of Geophysics*, *50*(2). https://doi.org/10.1029/2011rg000372

Cui, Y., Xu, C., Chen, H., Cui, Y., Xue, L., & Qin, S. (2025). Startup mechanism of locked segment–dominated rockslides: Insights from a physical model experiment replicating natural infiltration conditions. *Engineering Geology*, *108494*. https://doi.org/10.1016/j.enggeo.2025.108494

Dahal, R. K., & Hasegawa, S. (2008). Representative rainfall thresholds for landslides in the Nepal Himalaya. *Geomorphology*, *100*(3-4), 429-443. https://doi.org/10.1016/j.geomorph.2008.01.014

Dobriyal, P., Qureshi, A., Badola, R., & Hussain, S. A. (2012). A review of the methods available

for estimating soil moisture and its implications for water resource management. *Journal of Hydrology*, *458*, 110-117. https://doi.org/10.1016/j.jhydrol.2012.06.021

Dong, J., & Ochsner, T. E. (2018). Soil texture often exerts a stronger influence than precipitation on mesoscale soil moisture patterns. *Water Resources Research*, *54*(3), 2199-2211. https://doi.org/10.1002/2017WR021692

Dymond, S. F., Wagenbrenner, J. W., Keppeler, E. T., & Bladon, K. D. (2021). Dynamic hillslope soil moisture in a Mediterranean montane watershed. *Water Resources Research*, *57*(11), e2020WR029170. https://doi.org/10.1029/2020WR029170

Entin, J. K., Robock, A., Vinnikov, K. Y., Hollinger, S. E., Liu, S., & Namkhai, A. (2000). Temporal and spatial scales of observed soil moisture variations in the extratropics. *Journal of Geophysical Research: Atmospheres*, *105*(D9), 11865-11877. https://doi.org/10.1029/2000jd900051

Fang, X., Zhao, W., Wang, L., Feng, Q., Ding, J., Liu, Y., & Zhang, X. (2016). Variations of deep soil moisture under different vegetation types and influencing factors in a watershed of the Loess Plateau, China. *Hydrology and Earth System Sciences*, *20*(8), 3309-3323. https://doi.org/10.5194/hess-20-3309-2016, 2016

Gao, J., Shi, Y., Zhang, H., Chen, X., Zhang, W., Shen, W., Xiao, T., Zhang, Y. (2022). China regional 250m fractional vegetation cover data set (2000-2024). National Tibetan Plateau / Third Pole Environment Data Center. https://doi.org/10.11888/Terre.tpdc.300330. https://cstr.cn/18406.11.Terre.tpdc.300330

Ghannam, K., Nakai, T., Paschalis, A., Oishi, C. A., Kotani, A., Igarashi, Y., ... & Katul, G. G. (2016). Persistence and memory timescales in root-zone soil moisture dynamics. *Water Resources Research*, *52*(2), 1427-1445. https://cstr.cn/10.1002/2015wr017983

Hansun, S. (2013, November). A new approach of moving average method in time series analysis. In 2013 conference on new media studies (*CoNMedia*) (pp. 1-4). IEEE. https://doi.org/10.1109/conmedia.2013.6708545

Hersbach, H., Comyn-Platt, E., Bell, B., Berrisford, P., Biavati, G., Horányi, A., Muñoz Sabater, J., Nicolas, J., Peubey, C., Radu, R., Rozum, I., Schepers, D., Simmons, A., Soci, C., Dee, D., Thépaut, J.-N., Cagnazo, C., & Cucchi, M. (2023). ERA5 post-processed daily-statistics on

pressure levels from 1940 to present. Copernicus Climate Change Service (C3S) Climate Data Store (CDS). https://doi.org/10.24381/cds.4991cf48

Huang, F., Chen, J., Liu, W., Huang, J., Hong, H., & Chen, W. (2022). Regional rainfall-induced landslide hazard warning based on landslide susceptibility mapping and a critical rainfall threshold. *Geomorphology*, *408*, 108236. https://doi.org/10.1016/j.geomorph.2022.108236

Hu, W., Xu, Q., Wang, G. H., Van Asch, T. W. J., & Hicher, P. Y. (2015). Sensitivity of the initiation of debris flow to initial soil moisture. *Landslides*, *12*(6), 1139-1145. https://doi.org/10.1007/s10346-014-0529-2

Kantelhardt, J. W., Koscielny-Bunde, E., Rybski, D., Braun, P., Bunde, A., Havlin, S., 2006. Long-term persistence and multifractality of precipitation and river runoff records. *Journal of Geophysical Research: Atmospheres*, *111*(D1). https://doi.org/10.1029/2005jd005881

Kantelhardt, J. W., Koscielny-Bunde, E., Rego, H. H., Havlin, S., & Bunde, A. (2001). Detecting long-range correlations with detrended fluctuation analysis. *Physica A: Statistical Mechanics and its Applications*, *295*(3-4), 441-454. https://doi.org/10.1016/s0378-4371(01)00144-3

Kirchner, J. W. (2009). Catchments as simple dynamical systems: Catchment characterization, rainfall-runoff modeling, and doing hydrology backward. *Water Resources Research*, *45*(2). https://doi.org/10.1029/2008wr006912

Kim, S. (2015). ppcor: an R package for a fast calculation to semi-partial correlation coefficients. *Communications for statistical applications and methods*, *22*(6), 665.

Kursa, M. B., Jankowski, A., & Rudnicki, W. R. (2010). Boruta–a system for feature selection. *Fundamenta informaticae*, *101*(4), 271-285. https://doi.org/10.3233/FI-2010-288

Liu, S., van Meerveld, I., Zhao, Y., Wang, Y., & Kirchner, J. W. (2023). Seasonal dynamics and spatial patterns of soil moisture in a loess catchment. *Hydrology and Earth System Sciences Discussions*, *2023*, 1-26. https://doi.org/10.5194/hess-28-205-2024, 2024

Martínez-Fernández, J., González-Zamora, A., & Almendra-Martín, L. (2021). Soil moisture memory and soil properties: An analysis with the stored precipitation fraction. *Journal of Hydrology*, *593*, 125622. https://doi.org/10.1016/j.jhydrol.2020.125622

McColl, K. A., Alemohammad, S. H., Akbar, R., Konings, A. G., Yueh, S., & Entekhabi, D. (2017). The global distribution and dynamics of surface soil moisture. *Nature Geoscience*, *10*(2), 100-

104. https://doi.org/10.1038/ngeo2868

Mirus, B. B., Becker, R. E., Baum, R. L., & Smith, J. B. (2018). Integrating real-time subsurface hydrologic monitoring with empirical rainfall thresholds to improve landslide early warning. *Landslides*, *15*(10), 1909-1919. https://doi.org/10.1007/s10346-018-0995-z

Moragoda, N., Kumar, M., & Cohen, S. (2022). Representing the role of soil moisture on erosion resistance in sediment models: Challenges and opportunities. *Earth-Science Reviews*, *229*, 104032. https://doi.org/10.1016/j.earscirev.2022.104032

Nicolai-Shaw, N., Gudmundsson, L., Hirschi, M., & Seneviratne, S. I. (2016). Long-term predictability of soil moisture dynamics at the global scale: Persistence versus large-scale drivers. *Geophysical Research Letters*, *43*(16), 8554-8562. https://doi.org/10.1002/2016GL069847

Pan, H. L., Jiang, Y. J., Wang, J., & Ou, G. Q. (2018). Rainfall threshold calculation for debris flow early warning in areas with scarcity of data. *Natural Hazards and Earth System Sciences*, *18*(5), 1395-1409. https://doi.org/10.5194/nhess-18-1395-2018

Peng, C., Zeng, J., Chen, K. S., Li, Z., Ma, H., Zhang, X., ... & Bi, H. (2023). Global spatiotemporal trend of satellite-based soil moisture and its influencing factors in the early 21st century. *Remote Sensing of Environment*, *291*, 113569. https://doi.org/10.1016/j.rse.2023.113569

Rahmati, M., Amelung, W., Brogi, C., Dari, J., Flammini, A., Bogena, H., ... & Vereecken, H. (2024). Soil moisture memory: State-of-the-art and the way forward. *Reviews of Geophysics*, *62*(2), e2023RG000828. https://doi.org/10.1029/2023RG000828

Ran, Q., Su, D., Li, P., & He, Z. (2012). Experimental study of the impact of rainfall characteristics on runoff generation and soil erosion. *Journal of hydrology*, *424*, 99-111. https://doi.org/10.1016/j.jhydrol.2011.12.035

Parada, L. M., & Liang, X. (2003). A stochastic modeling approach for characterizing the spatial structure of L band radiobrightness temperature imagery. *Journal of Geophysical Research: Atmospheres*, *108*(D22). https://doi.org/10.1029/2003jd003567

Percival, D. B., & Walden, A. T. (1993). Spectral analysis for physical applications. cambridge university press.

Pickett, S. T. (1989). Space-for-time substitution as an alternative to long-term studies. In Long-

term studies in ecology: approaches and alternatives (pp. 110-135). New York, NY: Springer New York. https://doi.org/10.1007/978-1-4615-7358-6_5

Ponziani, F., Pandolfo, C., Stelluti, M., Berni, N., Brocca, L., & Moramarco, T. (2012). Assessment of rainfall thresholds and soil moisture modeling for operational hydrogeological risk prevention in the Umbria region (central Italy). *Landslides*, *9*(2), 229-237. https://doi.org/10.1007/s10346-011-0287-3

Rodriguez-Iturbe, I., Porporato, A., Ridolfi, L., Isham, V., & Coxi, D. R. (1999). Probabilistic modelling of water balance at a point: the role of climate, soil and vegetation. Proceedings of the Royal Society of London. *Series A: Mathematical, Physical and Engineering Sciences*, *455*(1990), 3789-3805. https://doi.org/10.1098/rspa.1999.0477

Salvucci, G. D., & Entekhabi, D. (1994). Equivalent steady soil moisture profile and the time compression approximation in water balance modeling. *Water Resources Research*, *30*(10), 2737-2749. https://doi.org/10.1029/94wr00948

Schönauer, M., Ågren, A. M., Katzensteiner, K., Hartsch, F., Arp, P., Drollinger, S., & Jaeger, D. (2024). Soil moisture modeling with ERA5-Land retrievals, topographic indices, and in situ measurements and its use for predicting ruts. *Hydrology and Earth System Sciences*, *28*(12), 2617-2633. https://doi.org/10.5194/hess-28-2617-2024, 2024

Schreiber, T., & Schmitz, A. (2000). Surrogate time series. Physica D: *Nonlinear Phenomena*, *142*(3-4), 346-382. https://doi.org/10.1016/s0167-2789(00)00043-9

Seneviratne, S. I., Corti, T., Davin, E. L., Hirschi, M., Jaeger, E. B., Lehner, I., ... & Teuling, A. J. (2010). Investigating soil moisture–climate interactions in a changing climate: A review. *Earth-Science Reviews*, *99*(3-4), 125-161. https://doi.org/10.1016/j.earscirev.2010.02.004

Song, P., Zhang, Y., Guo, J., Shi, J., Zhao, T., & Tong, B. (2022). A 1-km daily surface soil moisture dataset of enhanced coverage under all-weather conditions over China in 2003–2019. *Earth System Science Data Discussions*, *2022*, 1-51. https://doi.org/10.5194/essd-14-2613-2022

Van Genuchten, M. T. (1980). A closed-form equation for predicting the hydraulic conductivity of unsaturated soils. *Soil science society of America journal*, *44*(5), 892-898. https://doi.org/10.2136/sssaj1980.03615995004400050002x

Valavi, R., Elith, J., Lahoz-Monfort, J. J., & Guillera-Arroita, G. (2018). blockCV: An r package for

generating spatially or environmentally separated folds for k-fold cross-validation of species distribution models. *Biorxiv*, 357798. https://doi.org/10.1101/357798

Varga, C., & Csiszér, L. (2020). The influence of slope aspect on soil moisture. Acta Univ. Sapientiae Agric. *Environ*, *12*, 82-93. https://doi.org/10.2478/ausae-2020-0007

Wei, L., Song, D., Cui, P., Su, L., Zhou, G. G., Hu, K., ... & Tang, H. (2025). A long-term dataset of debris-flow and hydrometeorological observations from 1961 to 2024 at Jiangjia Ravine, China. *Earth System Science Data Discussions*, *2025*, 1-35. https://doi.org/10.5194/essd-2025-190

Western, A. W., Zhou, S. L., Grayson, R. B., McMahon, T. A., Blöschl, G., & Wilson, D. J. (2004). Spatial correlation of soil moisture in small catchments and its relationship to dominant spatial hydrological processes. *Journal of Hydrology*, *286*(1-4), 113-134. https://doi.org/10.1016/j.jhydrol.2003.09.014

Wicki, A., Jansson, P. E., Lehmann, P., Hauck, C., & Stähli, M. (2021). Simulated or measured soil moisture: which one is adding more value to regional landslide early warning?. *Hydrology and Earth System Sciences*, *25*(8), 4585-4610. https://doi.org/10.5194/hess-25-4585-2021

Wicki, A., Lehmann, P., Hauck, C., Seneviratne, S. I., Waldner, P., & Stähli, M. (2020). Assessing the potential of soil moisture measurements for regional landslide early warning. *Landslides*, *17*(8), 1881-1896. https://doi.org/10.1007/s10346-020-01400-y

Xie, P., Joyce, R., Wu, S., Yoo, S.-H., Yarosh, Y., Sun, F., & Lin, R. (2019). NOAA Climate Data Record (CDR) of CPC Morphing Technique (CMORPH) High Resolution Global Precipitation Estimates, Version 1 [indicate subset]. NOAA National Centers for Environmental Information. https://doi.org/10.25921/w9va-q159

Yang, H., Hu, K., Zhang, S., & Liu, S. (2023). Feasibility of satellite-based rainfall and soil moisture data in determining the triggering conditions of debris flow: The Jiangjia Gully (China) case study. *Engineering Geology*, *315*, 107041. https://doi.org/10.1016/j.enggeo.2023.107041

Yin, L., Dai, E., Zheng, D., Wang, Y., Ma, L., & Tong, M. (2020). What drives the vegetation dynamics in the Hengduan Mountain region, southwest China: Climate change or human activity?. *Ecological Indicators*, *112*, 106013. https://doi.org/10.1016/j.ecolind.2019.106013

Zhang, J., Wu, Z., Li, Y., Qin, C., & Cui, J. (2025). Memory character and predictive period of soil moisture in the root-zone and along hillslope. *Journal of Hydrology*, 133428.

https://doi.org/10.1016/j.jhydrol.2025.133428

Zhang, B., Tian, L., He, C., & He, X. (2023). Response of erosive precipitation to vegetation restoration and its effect on soil and water conservation over China's Loess Plateau. *Water Resources Research*, *59*(1), e2022WR033382. https://doi.org/10.1029/2022WR033382

Zhang, J. (2025). Daily Soil Moisture and Its Driving Factors (Static and Dynamic) in Three Watersheds: Dali River Basin, Anning River Basin, and Jiangjia Ravine (2003-2022) [Data set]. Zenodo. https://doi.org/10.5281/zenodo.17510469

Zhang, J. (2025). Code for: "Scale-Dependent Soil Moisture Memory and Its Driving Mechanisms in Hazard-Prone Mountain Watersheds". Zenodo. https://doi.org/10.5281/zenodo.17510622

Zhang, J., Li, Y., Yang, T., Liu, D., Liu, X., & Jiang, N. (2021). Spatiotemporal variation of moisture in rooted-soil. *Catena*, *200*, 105144. https://doi.org/10.1016/j.catena.2021.105144

Zhu, X., Fraedrich, K., Liu, Z., & Blender, R. (2010). A demonstration of long-term memory and climate predictability. *Journal of Climate*, *23*(18), 5021-5029. https://doi.org/10.1175/2010JCLI3370.1